UNIVERSITY OF HELSINKI REPORT SERIES IN PHYSICS

HU-P-D236

INELASTIC X-RAY SCATTERING STUDIES OF TRANSITION METAL COMPOUNDS

Kari Ruotsalainen

Division of Materials Physics
Department of Physics
Faculty of Science
University of Helsinki
Helsinki, Finland

ACADEMIC DISSERTATION

To be presented, with the permission of the Faculty of Science of the University of Helsinki, for public examination in the lecture hall LS1 of the Chemicum building of the University of Helsinki, A. I. Virtasen aukio 1, on the 8th of April 2016 at 12.15

Helsinki 2016

Supervisors

Simo Huotari, Ph. D.
Department of Physics
University of Helsinki
Helsinki, Finland

Professor Keijo Hämäläinen
Department of Physics
University of Helsinki
Helsinki, Finland

Pre-examiners

Professor Martti Puska
Department of Applied Physics
Aalto University
Espoo, Finland

Nozomu Hiraoka, Ph. D.
NSRRC National Synchrotron
Radiation Research Center
Hsinchu, Taiwan

Opponent

Christian Sternemann, Ph. D.
Technical University of Dortmund
Dortmund, Germany

Custos

Professor Keijo Hämäläinen
Department of Physics
University of Helsinki
Helsinki, Finland

Report Series in Physics HU-P-D236
ISSN 0356-0961
ISBN 978-951-51-1576-8 (printed version)
ISBN 978-951-51-1577-5 (pdf version)
http://ethesis.helsinki.fi/
Helsinki University Print
Helsinki 2016

Acknowledgements

Professors Juhani Keinonen and Hannu Koskinen are acknowledged for giving me the opportunity to pursue graduate studies at the Department of Physics of the University of Helsinki. The knowledge and wisdom on physics and the world of science passed on to me by Professor Keijo Hämäläinen and Dr. Simo Huotari who acted as my supervisors is greatly appreciated. The encouragement I've received from you has also been an important factor in the birth of this thesis. I must also mention how much I value the lessons learnt on how to work fast and efficient on a beamtime. Dr. Mikko Hakala is also acknowledged for guiding parts of my work involving computational physics. Dr. Johannes Niskanen, Dr. Antti Kettunen and M. Sc. Aki Kallonen are acknowledged for all the interesting discussions and fun times we've had. I also thank the rest of the X-ray laboratory staff for creating a workplace with a pleasant atmosphere. Finally, I wish express my gratitude to my close ones and friends for putting up with me for all these years.

K. Ruotsalainen

Abstract

Inelastic X-ray scattering spectroscopies form a versatile family of experimental techniques that are capable of probing the ground state properties as well as the single-particle and collective excitations of condensed-matter systems. Electronic excitations are of fundamental importance in determining the optical and transport properties of solids and also take part in the screening of the Coulomb interaction, thus contributing to ground-state properties. Transition-metal and rare-earth compounds exhibit a large variety of physical phenomena such as metal-insulator transitions, colossal magnetoresistance, unconventional magnetic ground states etc. These compounds are of fundamental and applied interest due to challenges in their theoretical description and their potential use in various devices ranging from transistors to infrared detectors.

This thesis presents four applications of inelastic X-ray scattering methods in transition-metal and rare-earth oxides as well as transition-metal dichalcogenides. First, we demonstrate that valence excitations in 55-nm-thick $LaAlO_3/SrTiO_3$ heterostructures can be measured. The data is analyzed utilizing free-ion multiplet and first-principles calculations. Second, it is demonstrated that the electron momentum-density difference across the metal-insulator phase transition in VO_2 is observable using the Compton-scattering spectroscopy, which probes the electronic ground state. The experimental results are compared against first-principles calculations. Third, a new experimental resonant X-ray emission method that utilizes a X-ray standing wave to excite the resonant scattering process is demonstrated using a $Gd_3Ga_5O_{13}$ single crystal. The method is shown to be very sensitive to quadrupole excitations. Its potential in achieving atomic-site sensitivity and electronic-state symmetry selectivity are discussed. Last, a joint experimental and computational study on the high-energy plasmon excitations in the transition-metal dichalcogenides $Cu_{0.2}NbS_2$ and $NbSe_2$ is presented. The primary significance of the first three studies lies in in demonstrations of new types of experiments, with several interesting possible applications in solid-state physics and materials science. The last study contributes to the discussion on the optical properties of transition-metal dichalcogenides.

Classification (IUPAP 2010): 71, 71.45.GM, 78.70.-g

Keywords: inelastic x-ray scattering, x-ray spectroscopy, transition metal compounds, electronic structure

Cover photo: KR

List of published articles

Paper I

K. O. Ruotsalainen, C. J. Sahle, T. Ritschel, J. Geck, M. Hosoda, C. Bell, Y. Hikita, H. Y. Hwang, T. T. Fister, R. A. Gordon, K. Hämäläinen, M. Hakala, S. Huotari, *Inelastic X-ray scattering in heterostructures: electronic excitations in* $LaAlO_3/SrTiO_3$. J. Phys. Cond. Mat. **27** (2015) 335501. The author contributed to the experiment and data-analysis, performed the first principles calculations, and wrote the majority of the paper.

Paper II

K. O. Ruotsalainen, J. Inkinen, T. Pylkkänen, T. Buslaps, K. Hämäläinen, M. Hakala, S. Huotari, *The isotropic Compton profile difference across the phase transition of* VO_2. Submitted to J. Phys. Chem. Sol. (2015). The author contributed to experimental work, data analysis, first principles calculations and wrote the paper.

Paper III

K. O. Ruotsalainen, A-P. Honkanen, S. P. Collins, G. Monaco, M. Moretti Sala, M. Krisch, K. Hämäläinen, M. Hakala, S. Huotari, *Resonant X-ray Emission With a Standing Wave Excitation.* Scientific Reports **6** (2016) 22648. The author concieved the experiment, contributed to experimental work and data analysis and wrote the majority of the manuscript.

Paper IV

P. Cudazzo, K. O. Ruotsalainen, C. J. Sahle, A. Al-Zein, H. Berger, E. Navarro-Moratalla, S. Huotari, M. Gatti, A. Rubio, *High-energy collective electronic excitations in layered transition-metal dichalcogenides* Phys. Rev. B **90** (2015) 125125 The author contributed to experimental work and data analysis, and wrote parts of the paper.

Other publications

I. Juurinen, T. Pylkkänen, K. O. Ruotsalainen, C. J. Sahle, G. Monaco, K. Hämäläinen, S. Huotari, M. Hakala, *Saturation Behavior in X-ray Raman Scattering Spectra of Aqueous LiCl.* J. Phys. Chem. B **117** (2013) p. 16506–16511.

J. Inkinen, A. Sakko, K. O. Ruotsalainen, T. Pylkkänen, S. Galambosi, M. Hakala, G. Monaco, S. Huotari, K. Hämäläinen, *Temperature dependence of* CO_2 *and* N_2 *core-*

electron excitation spectra at high pressure. PCCP **15** (2013) p. 9231–9238.

J. Inkinen, J. Niskanen, A. Sakko, K. O. Ruotsalainen, T. Pylkkänen, S. Galambosi, M. Hakala, G. Monaco, K. Hämäläinen, S. Huotari, *Interplay between Temperature-Activated Vibrations and Nondipolar Effects in the Valence Excitations of the CO_2 Molecule.* J. Phys. Chem. A **118** (2014) p. 3288–3294.

J. Koskelo, I. Juurinen, K. O. Ruotsalainen, M. J. McGrath, I-F. Kuo, S. Lehtola, S. Galambosi, K. Hämäläinen, S. Huotari, M. Hakala, *Intra- and intermolecular effects on the Compton profile of the ionic liquid 1,3-dimethylimidazolium chloride.* J. Chem. Phys. **41** (2014) 244505.

J. Niskanen, C. J. Sahle, K. O. Ruotsalainen, H. Müller, M. Kavcic, M. Zitnik, K. Bucar, M. Petric, M. Hakala, S. Huotari, *Sulphur K_β emission spectra reveal protonation states of aqueous sulfuric acid.* Scientific Reports **6** (2016) 21012

Contents

1 Introduction

The electronic structure of matter is a subject of widespread interest and numerous unresolved problems. By electronic structure one refers to the organisation of well bound electrons in the vicinity of atomic nuclei, valence electrons in chemical bonds, and unbound charge carriers in conducting systems. Condensed phases of nuclei and electrons and their transport and mechanical properties form the basis of modern technological society. Physical understanding of various phenomena in solids advanced rapidly with the application of the methods of quantum mechanics, quantum-field theory and statistical physics. [1,2] Despite triumphs in explaining and even quantitatively predicting properties of simple metals and semiconductors, the electronic structure and properties of e.g. many transition-metal and rare-earth oxides remain a challenge to theoretical models due to many-body effects associated with partially filled and spatially localized electron states leading to so-called strong electron correlation. [3, 4] To take steps further, spectroscopic experiments that use scattering, absorption and emission of X-rays reveal detailed information such as energy levels and occupations of electronic states. The interpretation of such experiments also requires theoretical understanding of the probed material and the excitation process in order to reach reliable conclusions. Thus the union of experiment and theory is particularly important in spectroscopy and crucial for advancing condensed-matter physics and related disciplines.

After the discovery of X-rays, their applicability in studying matter became quickly apparent with the demonstration of X-ray imaging. [5] Diffraction of X-rays by long-range-ordered crystalline matter allowed analysis of the atomic structure. The element-specificity of X-ray emission provided a method for analyzing the elemental content. First steps in the topic of this thesis, inelastic X-ray scattering (IXS), were taken and provided proof for the quantum nature of light and for the validity of Fermi-Dirac statistics for electrons over the Maxwell-Boltzmann distribution. [6, 7] Several refined experimental techniques were developed using traditional X-ray tubes and radionuclide based sources, but these were often experimentally difficult demonstrations. (e.g. Ch. 4 in Ref. [7]) Widespread applications had to wait until dedicated synchrotron-radiation facilities were established and provided powerful light beams with tunable energy and polarization. Regular X-ray absorption and emission (XAS and XES) experiments were and are performable with X-ray tubes [8], albeit synchrotrons are indispensable for many of their modern applications. Some delicate studies of e.g. magnetism with XAS may also require the utilization of the polarized radiation provided by a synchrotron. IXS spectroscopies are a branch of experimental methods where modern synchrotron facilities have made experiments that were previously very challenging, or even impossible, into reality. Especially some results presented later on in this thesis have been facilitated by quite recent improvements in synchrotron-radiation sources and experimental setups.

The fundamental quantities of IXS are the energy transfer $\hbar\omega$ and the momentum transfer $\hbar\mathbf{q}$ between a photon and a scattering target. As the photon loses energy in the scattering process, the target is left in an excited state. We thus learn how the system is able to absorb and dissipate energy by measuring the IXS cross section as a function of $\hbar\omega$. [9] The excitation modifies the distribution of electrons in the target. If the disturbance is able to propagate, it is manifested in a momentum-transfer dependence of the excitation energy, i.e. dispersion. The nature of the excitations depends on the target material and some types of excitations are only observable for certain momentum transfers. Roughly sketched, one can identify single-particle and collective excitations involving the nuclei (lattice vibrations), electrons and electron spins, or combinations thereof. Ignoring the nuclear and spin degrees of freedom, electronic single-particle transitions include e.g. interband and intraband transitions and excitations into continuum states. Bound electron-hole pairs known as excitons are also observable. Electronic collective transitions include collective high frequency oscillations of the valence electrons, plasmons. [9]

Resonant X-ray emission spectroscopy (RXES) involves tuning the incident photon wavelength across a core electron absorption threshold and measuring the resonantly excited X-ray emission originating from an occupied core level. In conventional XAS one can reveal e.g. the energies and symmetries of unoccupied electron states. The XAS spectrum is broadened by the lifetime of the final-state core hole and sometimes spectral features sensitive to e.g. magnetism and the local chemical environment may be masked by this effect. High-resolution RXES provides a way to overcome this limitation, and can be used to investigate the electronic states accessed by XAS in greater detail. [9–12] The RXES cross section is however more challenging to evaluate theoretically as the process takes place via intermediate electronically excited states.

The materials studied with IXS and RXES in this thesis have been transition-metal and rare-earth metal oxides (VO_2, $LaAlO_3$, $SrTiO_3$, $Gd_3Ga_5O_{13}$) and chalcogenides ($Cu_{0.2}NbS_2$, $NbSe_2$) abbreviated TMO, REO and TMDC. The first two categories often have extraordinary properties which are not accounted for by the commonly utilized methods of electronic-structure theory. This is due to the many-body effects mentioned in the beginning of this section. Metal-insulator transitions (MIT) and unconventional superconductivity are typical examples of the effects of electron correlations in TMOs. [3,13–15] In some TMOs the coupling of phonons with electronic degrees of freedom lead into e.g. ferroelectric and magnetoresistive phenomena. [3] Thus a notable characteristic of TMOs are the rich phase diagrams as a function of e.g. chemical doping, pressure, temperature and external electromagnetic field.

Two systems that exhibit a MIT were studied in the work presented later on. VO_2 exhibits an interesting MIT as the transition is accompanied by a structural phase transition, and there are three distinct insulating states that can be accessed by replacing V with Cr up to 0.25 %. [3,16] Interfaces of $LaAlO_3$ (LAO) and $SrTiO_3$ (STO),

both good insulators in bulk form, prepared under specific conditions also exhibit a MIT. [17] Apart from the aforementioned TMOs, the REO $Gd_3Ga_5O_{13}$ (GGG) was used as an test case to demonstrate an methodological advance in obtaining site selectivity in RXES. The electronic properties of REOs are also of general interest due to e.g. exotic magnetic ground states [18]. TMDCs have been studied extensively in recent years, in large part due to the discovery of mono- and few-layer compounds with promising applications in electronics and optoelectronics. [19] Some TMDCs also exhibit charge-density-wave order at low temperatures and a transition to a superconducting state at very low temperatures below 10 K. [20, 21]

This thesis is organized as follows. In Ch. 2 The fundamentals of electronic structure theory, radiation matter interaction, response functions measured by IXS, and the cross section for RXES are discussed. The basic results of dynamical X-ray diffraction theory are also presented to elucidate the results of paper III. In Ch. 3 I present the experimental methods utilized this thesis ranging from the radiation source to the scattered energy analysis, and also present the beamlines utilized in this work. In Ch. 4 I summarize the motivations, methods and results of the associated publications. Finally, Ch. 5 contains my concluding remarks. The papers are reprinted in appendices I-IV.

2 Theoretical background

Atomic Hartree units are used in formulae throughout this section with the exception of the discussion on dynamical diffraction theory, where SI units following Ref. [22] are used. Boldface symbols denote vector quantities and carets are used to mark operators.

2.1 Electronic structure theory

The interpretation of spectroscopic experiments demands comparison to theoretical results since the precise nature of the involved electronic states and excitation mechanisms are not known beforehand, although general rules of thumb do exist for e.g. energies of certain excitations. The first step to understand a spectrum is to study the ground-state electronic structure of the system, given by the Hamiltonian operator and its eigenfunctions and values. The time-independent non-relativistic Hamiltonian for a system of nuclei and electrons can be written down as [4]

$$\hat{H} = \hat{T}_n + \hat{V}_{nn} + \hat{V}_{ne} + \hat{T}_e + \hat{V}_{ee}. \tag{1}$$

The terms of the Hamiltonian operator are the nuclear kinetic energy $\hat{T}_n = -\frac{1}{2}\sum_i \frac{\nabla_i^2}{M_i}$, nucleus-nucleus Coulomb interaction $\hat{V}_{nn} = \frac{1}{2}\sum_{i\neq j} \frac{Z_i Z_j}{|\mathbf{R_i}-\mathbf{R_j}|}$, nucleus-electron Coulomb interaction $\hat{V}_{ne} = -\frac{1}{2}\sum_{i,j} \frac{Z_j}{|\mathbf{r_i}-\mathbf{R_j}|}$, electron kinetic energy $\hat{T}_e = -\frac{1}{2}\sum_i \nabla_i^2$ and the electron-electron Coulomb interaction $\hat{V}_{ee} = \frac{1}{2}\sum_{i\neq j} \frac{1}{|\mathbf{r_i}-\mathbf{r_j}|}$. Z denotes the nuclear charge, M the nuclear mass and upper (lower) case vectors the nuclear (electron) coordinates. The summations run over all particles in the system and self-interactions are excluded. The many-body wave function is denoted $\Psi(\{\mathbf{R_i}\},\{\mathbf{r_j}\})$, where the indices run over all nuclei and electrons. The wavefunction is antisymmetric with respect to permutation of fermion coordinates to satisfy the Pauli principle.

In the calculations presented in the papers mean-field theory methods, in which each electron interacts with the average field of the other electrons, are applied. [4, 23] The wave function is approximated with a single Slater determinant constructed from the wave functions $\psi^\sigma(\mathbf{r_i})$, where $\mathbf{r}$ is a position variable and σ is the spin. Further simplification is achieved by adopting the Born-Oppenheimer approximation and setting $\hat{T}_n = 0$. [4] The electronic part of the Hamiltonian and the $\hat{V}_{ne}$ term then depends parametrically on the nuclear coordinates. In the Hartree-Fock approximation, the electron-electron interaction is approximated by the direct Hartree $\hat{V}_H$ term, representing the classical electrostatic interaction between charges, and exchange $\hat{V}_X$ term acting, on the single particle states. [4] In this thesis the Kohn-Sham density-functional theory (KS-DFT) is utilized. [24, 25] The basic idea of KS-DFT is to treat the many-body problem using an effective single-particle problem, where the density constructed from a non-interacting auxiliary single-particle system reproduces the exact interacting electronic density. [25] The total energy of the system can then be written

as a universal (i.e. material independent) functional of the electron density. [24, 25] Electron-electron interaction effects beyond the Hartree term are expressed in terms of an exchange-correlation potential V_{xc}. Approximations for V_{xc} are numerous in principles and methods of construction. [26, 27] The local-density and local-spin-density approximations (LDA/LSDA) are used in this work. [26] In these approximations the exchange-correlation potential at each point in space $\mathbf{r}$ is taken to be the same as in an interacting homogeneous electron gas of the corresponding (spin) density derived from quantum Monte Carlo calculations. [26, 28] The LDA+U approximation is also utilized, in which an effective local potential U for electrons of opposite spin (i.e. the local Coulomb interaction in the Hubbard model $\hat{H}_{int,H} = U \sum_i n_{i,\uparrow} n_{i,\downarrow}$ [14, 29], where the n_i are occupation numbers) is applied to a selected subsets of electron states to mimic the effect of strong electron correlation. [29]

The Kohn-Sham equations for the single-particle states can be solved numerically in a given basis even for complex materials with dozens or hundreds of atoms in the unit cell. Here the basis is always taken to consist of Bloch states $\psi_{n,\mathbf{k}}(\mathbf{r}) = u_{n,\mathbf{k}}(\mathbf{r}) e^{i\mathbf{k}\cdot\mathbf{r}}$ in an infinite solid, where the function $u_{n,\mathbf{k}}(\mathbf{r})$ has the periodicity of the unit cell. [30] Further approximations are made for practical calculations. The norm-conserving pseudopotential method as implemented in the ABINIT code was used in paper I. [31] In this method, deep core levels are taken out of the electronic problem and their effect on the valence electrons is mimicked by a pseudopotential that behaves smoothly near the nuclei, which allows for a smaller plane-wave basis to be used. [4] In practice the pseudopotential method corresponds to selecting the valence-electron subset from the corresponding atomic all-electron problem, and angular-momentum independent (or dependent) pseudization radii for different electron states. [32–34] Inside the relevant radius, the pseudopotential and the associated pseudo wave functions are forced to be smooth, and to match the all-electron potential and wave function at the boundary. In this work, the Hartwigensen-Goedecker-Hutter pseudopotentials were utilized in paper I. [33]

Very accurate mean-field-theory methods are based on a augmented plane wave basis. [35] Here this method was used in paper II as implemented in the Elk code. [36] The core electrons can be kept in the calculation by partitioning the space to regions near nuclei, so-called muffin-tin spheres, and the interstitial region. In the full-potential linearized augmented-plane-wave method, a radial Schrödinger or a corresponding relativistic wave equation is solved within the muffin-tin spheres and the basis inside the sphere consists of localized radial functions centered on the nuclear positions, and their energy derivatives. [4, 37] Outside the sphere, plane-wave states are used. The solutions are matched at the boundary of the spheres and the interstitial region by using continuity of the wave function and its derivatives for different angular momenta.

More advanced theoretical models are also available for calculations on real materials. The Kohn-Sham scheme can be generalized to include an orbital-dependent V_{xc},

which in practice corresponds to an inclusion of the Hartree-Fock exchange in the KS Hamiltonian. [38] Two other prominent methods for solids are based on a Green's function treatment of the many-body problem. [1, 2] The many-body effects are brought to the form of a self-energy operator. [39–41] The GW method is based on many-body perturbation theory, and in essence is a screened Hartree-Fock approximation for the one electron Green's function with a self-energy operator that is the product of the Green's function G and the screened interaction W. [39–41] The perturbative G^0W^0 method provides accurate values for various observable for simple metals and semiconductors. [41, 42] Dynamical mean field theory (DMFT) is also a Green's function based theory, which seeks to fully account for the local Coulomb interaction on a given (transition metal) atomic site by solving for a local frequency-dependent Green's function, while treating the rest of the electrons in static mean field approximation (e.g. DFT). [43] DMFT calculations have been shown to capture features of the properties of transition-metal-oxide materials such as metal-insulator transitions, but they necessarily miss nonlocal effects of the electron-electron interaction in a single site approximation. [43, 44]

2.2 X-ray interactions with matter

The interaction of radiation and matter can be described with the time-dependent perturbation theory. [9, 45, 46] Only the charge-scattering terms are presented here, since magnetic scattering is not utilized in this thesis and the corresponding terms in the interaction Hamiltonian are small. A photon with wave vector $\mathbf{K}$, polarization vector $\mathbf{e}$ and energy ω is represented by a second-quantized photon field (in a quantization volume Ω),

$$\hat{\mathbf{A}}(\mathbf{r},t) = \sum_{\mathbf{K},\lambda} \left(\frac{2\pi}{\alpha^2\Omega\omega}\right)^{\frac{1}{2}} \left[\hat{c}(\mathbf{K},\lambda)\mathbf{e}(\mathbf{K},\lambda)\mathrm{e}^{i\mathbf{K}\cdot\mathbf{r}-i\omega\cdot t} + \hat{c}^\dagger(\mathbf{K},\lambda)\mathbf{e}(\mathbf{K},\lambda)\mathrm{e}^{-i\mathbf{K}\cdot\mathbf{r}+i\omega\cdot t}\right], \quad (2)$$

where λ is an index running over the polarization states, $\hat{c}^\dagger$ ($\hat{c}$) is the photon creation (annihilation) operator. The quantized vector potential operator $\hat{\mathbf{A}}(\mathbf{r},t)$ is introduced to the electronic Hamiltonian via the so-called minimal substitution $\hat{\mathbf{p}} \rightarrow \hat{\mathbf{p}} - \alpha\hat{\mathbf{A}}$, where α is the fine structure constant. [46] First-order time-dependent perturbation theory gives that the XAS transition rate $W_{gf}(\omega)$ from initial state $|g\rangle$ to final state $|f\rangle$ is proportional to (Ref. [46])

$$W_{gf}(\omega) \propto \alpha \left| \langle f | \sum_j \hat{\mathbf{A}}(\mathbf{r}_j,t)\cdot\hat{\mathbf{p}}_j |g\rangle \right|^2 \delta(E_f - E_g - \omega). \quad (3)$$

The initial state is the electronic ground state and the final state is a core-excited state. The XES transition rate from a core-excited initial state is calculated using $\mathbf{p}_j \cdot \hat{\mathbf{A}}(\mathbf{r}_j,t)$

as the transition operator in Eq. 3. The IXS and RXES cross sections are calculated using a similar expression in second order time dependent perturbation theory, known as the Kramers-Heisenberg formula (Ref. [9]):

$$\frac{\mathrm{d}^2\sigma}{\mathrm{d}\Omega\mathrm{d}\omega} = \alpha^2\frac{\omega_2}{\omega_1}\Bigg| \langle f| \sum_j \mathrm{e}^{i\mathbf{q}\cdot\mathbf{r}_j} |g\rangle \, (\mathbf{e}_1\cdot\mathbf{e}_2) + \sum_n \sum_{j,j'} \left(\frac{\langle f| \, \mathbf{e}_2\cdot\mathbf{p}_j \mathrm{e}^{i\mathbf{K}_2\cdot\mathbf{r}_j} |n\rangle \langle n| \, \mathbf{e}_1\cdot\mathbf{p}_{j'} \mathrm{e}^{i\mathbf{K}_1\cdot\mathbf{r}_{j'}} |i\rangle}{E_g - E_n + \omega_1 + i\Gamma_n/2} \right) \Bigg|^2 \delta(E_g - E_f + \omega). \quad (4)$$

The δ-function describes energy conservation in the scattering process and the index 1(2) corresponds to incident (scattered) photons. The electronic states involved are the ground state $|g\rangle$, intermediate state $|n\rangle$ and the final state $|f\rangle$ of the electron system. The first term describes non-resonant IXS and the second describes RXES. At the $\omega = 0$ limit the cross section reduces to the (resonant) elastic scattering cross section. The RXES term has several notable characteristics: i) the energy denominators become small in the vicinity of core absorption thresholds and enhance the scattering cross section, [9, 47] ii) the polarization dependence of the RXES term also allows studying the symmetries of the electronic states involved, [9] iii) the summation over the intermediate states results in interference effects, which can complicate understanding the cross section in comparison with the non-resonant XES.

The exponential term in Eq. 2 has an expansion of the form

$$\mathrm{e}^{i\mathbf{K}\cdot\mathbf{r}} \propto \sum_{L=0}^{\infty} \sum_{M=-L}^{M=L} J_L(\mathbf{r}) Y_L^M(\mathbf{K}), \quad (5)$$

where J_L is a spherical Bessel function and the Y_L^M are spherical harmonics. The multipole expansion of the photon field can be seen to give access to non-dipolar scattering channels, which is a notable feature of IXS as large momentum transfers are accessible with hard X-ray photons. [48] The dependence of the cross section on the magnitude and orientation of the momentum transfer is also useful for investigating the symmetries of the electron states involved in the transition. [49, 50]

2.3 Response functions in the valence excitation and Compton regimes

The IXS term in Eq. 4 can be written in terms of the dynamic structure factor (DSF)

$$S(\mathbf{q},\omega) = \Bigg| \langle f| \sum_j \mathrm{e}^{i\mathbf{q}\cdot\mathbf{r}_j} |g\rangle \Bigg|^2 \delta(E_g - E_f + \omega). \quad (6)$$

Due to the fluctuation-dissipation theorem, it is intimately connected to the linear-response density-density response function $\chi(\mathbf{q},\omega)$ by $S(\mathbf{q},\omega) \propto \operatorname{Im}\chi(\mathbf{q},\omega)$. [9] A second relation of importance is $S(\mathbf{q},\omega) = \frac{q^2}{4\pi^2}\operatorname{Im}\frac{-1}{\epsilon_M}$, where $\epsilon_M(\mathbf{q},\omega)$ is the macroscopic dielectric function and obtained from χ by

$$\frac{1}{\epsilon_M(\mathbf{q},\omega)} = 1 + v(\mathbf{q})\chi(\mathbf{q},\omega), \tag{7}$$

where $v(\mathbf{q})$ is the Fourier transform of the unscreened Coulomb interaction. The inverse dielectric function is also the screening function of the Coulomb interaction in many-body perturbation theory, and is an important quantity to study in fundamental investigations of many-body theory or applications of e.g. the GW approximation to material-specific questions. [1, 2, 40, 41]

The density-density response function χ can be calculated from first principles using the time-dependent DFT (TDDFT). [41, 51, 52] The dielectric function has to be inverted in the process of calculating the macroscopic linear-response properties. For solids the dielectric function is actually a matrix (i.e. has to represent the inhomogeneity of the electron system), the head element of which is ϵ_M. [41, 53–56] The matrix inversion gives rise to so-called local-field effects, which redistribute the excitation probabilities by coupling excitations differing in wave vector by a reciprocal lattice vector $\mathbf{G}$. [53, 55–58] Taking the matrix nature of the response functions into account the macroscopic dielectric function becomes $\epsilon_M(\mathbf{q},\omega) = 1/\epsilon^{-1}_{\mathbf{G}\mathbf{G}'}|_{\mathbf{G},\mathbf{G}'=0}$, and the linear-response Dyson equation for the matrix $\chi_{\mathbf{G},\mathbf{G}'}$ is

$$\chi_{\mathbf{G},\mathbf{G}'}(\mathbf{q},\omega) = \chi^0_{\mathbf{G},\mathbf{G}'} + \sum_{\mathbf{G}_1,\mathbf{G}_2} \chi^0_{\mathbf{G},\mathbf{G}_1}(\mathbf{q},\omega)\big[v(\mathbf{q})_{\mathbf{G},\mathbf{G}'} + f^{xc}_{\mathbf{G},\mathbf{G}'}(\mathbf{q},\omega)\big]\chi_{\mathbf{G}_2,\mathbf{G}'}(\mathbf{q},\omega), \tag{8}$$

where V is the Coulomb potential and f_{xc} is the exchange-correlation kernel in TDDFT. [41, 52, 59, 60] χ_0 is the non-interacting response function

$$\chi^0_{\mathbf{G},\mathbf{G}'}(\mathbf{q},\omega) = \frac{2}{\Omega}\sum_f \frac{F_g - F_f}{\omega + i\eta + E_g - E_f} \langle g| e^{i(\mathbf{q}+\mathbf{G})\cdot\mathbf{r}} |f\rangle \langle f| e^{i(\mathbf{q}+\mathbf{G}')\cdot\mathbf{r}} |g\rangle , \tag{9}$$

where the F is the Fermi occupation function, η a positive infinitesimal, Ω is the unit cell volume and the summation runs over the final states f. [59] It is also possible to include the electron-hole interaction in the response functions by utilising the Bethe-Salpeter equation. [41, 54, 61–64] In papers I and IV, the random phase approximation (RPA) with local-field effects is adopted. In the RPA, the f_{xc} term in Eq. 8 is set to zero, i.e. exchange and correlation effects on the response function are neglected. In paper I the YAMBO code was used. [65]

The macroscopic dielectric function gives access to the frequency-dependent optical functions of matter. [41] For example, the optical absorption spectrum is given by the imaginary part of ϵ_{M}. The dielectric function also provides a method for interpretation

of IXS experiments. Writing $\epsilon_M = \epsilon_1 + i\epsilon_2$, $-\operatorname{Im} 1/\epsilon_M = \epsilon_2^2/(\epsilon_1^2 - \epsilon_2^2)$, it is seen that one observes peaks at the zero crossings of ϵ_1, when ϵ_2 is small. These peaks correspond to plasmons with energy ω_p. [2,9] In the long-wave-length limit, peaks in ϵ_2 correspond to interband or single-particle transitions which are strong in optical absorption, and are also observable in IXS. The momentum dependence of the DSF is roughly characterized as follows. At low to intermediate momentum transfers and low energy transfers the DSF displays the interband, charge-transfer and plasmon excitations. When the momentum transfer is increased from small to intermediate values, the plasmons broaden due to coupling with the single-particle transitions. At large momentum transfers and low energy losses, non-dipolar transition matrix elements are enhanced and intrashell dd or ff excitations can be observed. [48] Bound excitons may also be observed, if the electronic structure supports them, i.e. if there is an energy gap and screening of the hole left in the valence band is incomplete.

In the limit of large energy and momentum transfers the DSF contains information on the momentum distribution of the electrons, and the corresponding regime of IXS is known as Compton scattering. [7] In this case, the IXS spectra are often analysed within the so-called impulse approximation (IA). The IA connects the $S(\mathbf{q}, \omega)$ to the electron momentum distribution $\rho(\mathbf{p})$ in the case $\omega \gg E_B$ and $q \gg 1/r_{avg}$, where E_B is characteristic binding energy scale and r_{avg} is the mean electron-electron distance. [66, 67] In these conditions, the DSF is directly proportional to the Compton profile

$$J(p_z) = \int\int \mathrm{d}p_x \mathrm{d}p_y \rho(\mathbf{p}). \tag{10}$$

Eq. 10 represents a projection of the 3D electron momentum density onto the scattering vector $\mathbf{q}$. In paper I the expression for p_z

$$p_z = q/2 - (\omega_1 - \omega_2)\big(1/4 + 1/[2\omega_1\omega_2(1 - \cos\theta)]\big)^{1/2} \tag{11}$$

is used to convert the scattered photon energy scale to the electron momentum scale. [68] The momentum distribution is a ground-state quantity and thus relatively straightforward to be calculated for a given electronic structure. [69] There are several aspects of Compton spectroscopy that are highly useful for electronic-structure studies: i) the $\rho(\mathbf{p})$ can reveal lengths of chemical bonds, i.e. give structural information [70], ii) for metallic systems, the Fermi-surface breaks may be located and a Fermi-surface map can be constructed [71, 72], iii) the second moment of the isotropic Compton profile is also proportional to the expectation value of the electron kinetic energy, and thus it is possible to determine energetics with Compton spectroscopy using the formula [73]

$$\left\langle p^2 \right\rangle = 6 \int \mathrm{d}p p^2 J(p). \tag{12}$$

The total energy can then be derived from the virial theorem. [73,74] This a notable feature of Compton spectroscopy, as it enables microscopic measurements of macroscopic thermodynamic quantities.

2.4 Resonant X-ray emission spectroscopy

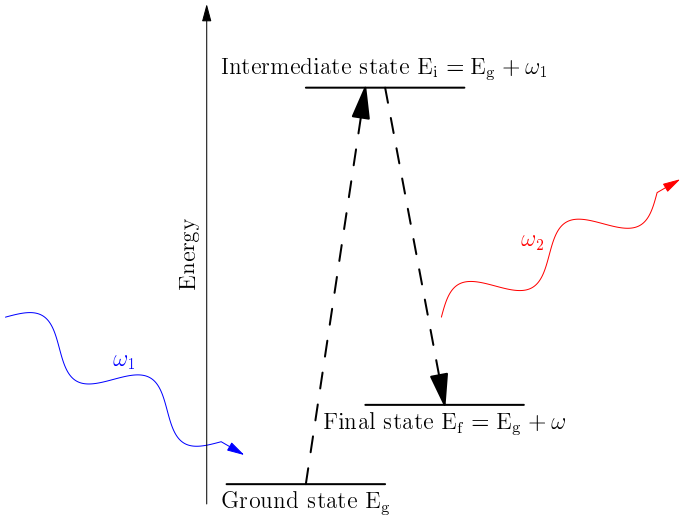

Figure 1: Energy level diagram depicting the RXES process. The electronic ground state with energy E_g absorbs a photon with energy ω_1. The intermediate state decays by emission of a photon with energy ω_2 and the final state energy is $E_f = E_g + \omega_1 - \omega_2$.

RXES is described by the second term in Eq. 4. In RXES a core electron is excited to an unoccupied state, followed by radiative decay from an occupied state as in Fig. 1. RXES can be considered as a variant of X-ray absorption spectroscopy, which yields more detailed information on the absorption edge fine structure. Neglecting matrix element effects, the RXES spectrum can be approximated by

$$I(\omega_1, \omega_2) = \int \mathrm{d}\epsilon \frac{\rho(\epsilon)\rho(\epsilon + \omega_1 - \omega_2)}{(\epsilon - E_B - \omega_2)^2 + \Gamma^2}, \tag{13}$$

where $\rho(\epsilon)$ and $\rho(\epsilon+\omega_1-\omega_2)$ are the densities of the occupied for the unoccupied states, respectively, and E_B the core electron binding energy. [47] The lifetime broadening factor in XAS is the final state lifetime. The broadening can in some cases obscure weak transitions. This causes complications in e.g. interpreting XAS experiments and different varieties of magnetic X-ray spectroscopies. [75–79] The lifetime broadening effect can be overcome with RXES, where one can observe an effective suppression of lifetime broadening if one focuses on measuring the intensity of a given emission line with sub-linewidth resolution. [10] The different intermediate states of RXES corresponding to the XAS final states may be resolved from the emission spectrum. [77, 78] The resonant excitation also provides symmetry selectivity via the absorption-emission process, and can be used to probe the spin polarization of unoccupied electron states. [9–12] Further selectivity over atomic site in the unit cell may be obtained if the absorption cross section has suitably separated resonances. [9, 12]

2.5 Dynamical theory of X-ray diffraction

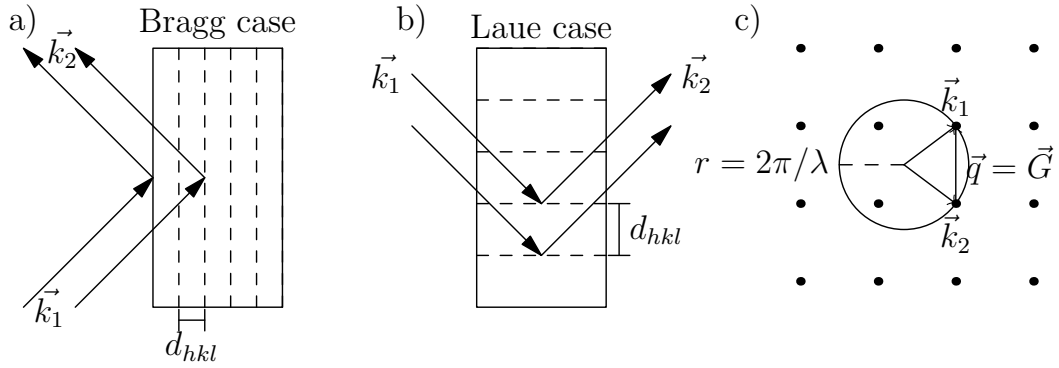

Figure 2: a) Visualisation of the diffraction geometry in the Bragg (reflection) case. The $\mathbf{k}_i$ describe the incident (1) and outgoing (2) wave-vector directions and d_{hkl} is the lattice-plane distance. b) The Laue (transmission) case. c) The Ewald sphere used to visualize the relations between the incident and diffracted waves with respect to the relevant reciprocal lattice. The points denote reciprocal lattice sites. The Laue condition for diffraction requires that the scattering vector $\mathbf{q}$ is a reciprocal lattice vector for diffraction to occur. The sphere has a radius of $|\mathbf{k}_i|$.

Dynamical theory of X-ray diffraction is essential for understanding how X-rays are diffracted in near perfect crystals, such as many optical elements in X-ray physics. [9] It also provides means for novel spectroscopies as reviewed in literature and is demonstrated later on in paper III. [80, 81] The experimental geometries in the Bragg and Laue (reflection and transmission) geometries is presented in Fig 2 a) and b). The dynamical theory is derived by taking interference of the coherently coupled incident and diffracted beams into account while solving the Maxwell equations for a periodic medium. [22] It takes into account refraction at the vacuum-crystal interface and corrects for the angular positions of Bragg peaks with respect to a straightforward application of Bragg's law. [22, 82] The allowed wave vectors for diffraction, angular width of the reflections and the spatial structure of the wave field are important in the context of this work and will be introduced next. An important underlying assumption of the following presentation is that the incident and scattered waves are described by plane waves, and that there are only two strong waves in the crystal, the incident and diffracted wave with wave vectors $\mathbf{K}_O$ and $\mathbf{K}_H$, respectively. The allowed wave vectors for diffraction to take place, for linear polarizations states, are expressed by finding the solutions for E_0 and E_H in

$$\begin{aligned} [k^2(1-\Gamma F_0) - (\mathbf{K}_0 \cdot \mathbf{K}_0)]E_O - k^2 P\Gamma F_{\bar{H}} E_H = 0 \\ -k^2 P\Gamma F_H E_O + [k^2(1-\Gamma F_0) - (\mathbf{K}_H \cdot \mathbf{K}_H)]E_H = 0 \end{aligned} \tag{14}$$

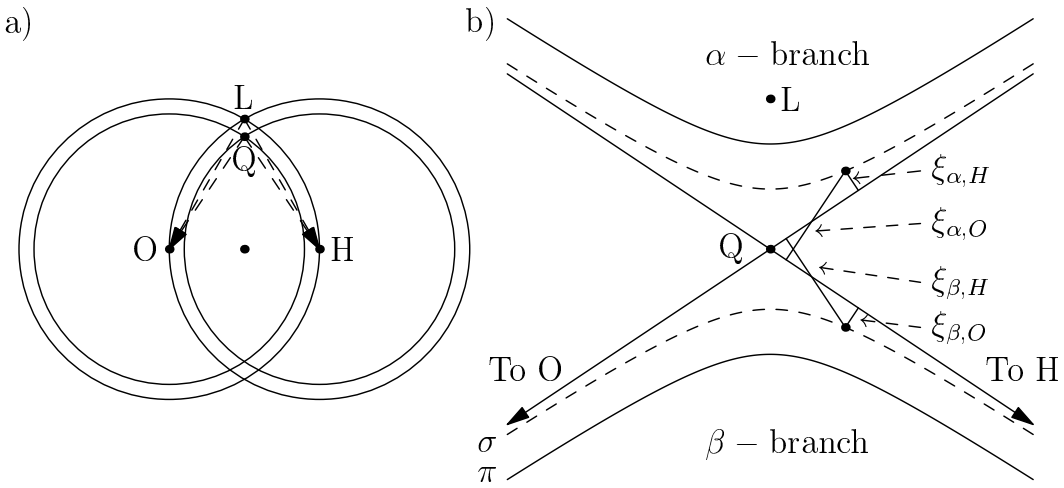

Figure 3: a) Reciprocal space depiction of diffraction. The radii of the circles drawn around the reciprocal lattice origin O and point H represent the in vacuum and in medium wave vectors. The vectors LO and LH correspond to the vacuum and L is denoted the Laue point. The vectors QO and QH correspond to the in medium waves and Q is denoted the Lorentz point. The scale is greatly exaggerated for visual clarity ($k_{med} = 0.9k_{vac}$, in real crystals the difference is of the order 10^{-6}). b) Zoom in of the intersection region near Q and L. The dispersion surfaces are the hyperbolic solid and dashed lines (π- and σ-polarization, respectively). A point on the dispersion surfaces is called a tie point (solid dot in figure), from which the incident and diffracted wave vectors start. The α-branch corresponds to waves with tie points closer to L than Q, and vica versa for the β-branch. The spheres about O and H are well approximated as straight lines in the intersection region. The ξ-parameters describe distances from the tie point to the Ewald spheres.

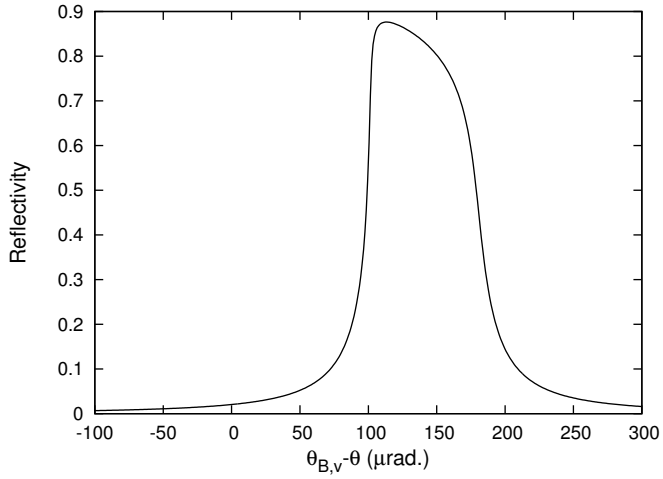

Figure 4: The rocking curve of the Si(533) reflection for $\lambda = 1.6531\mathring{A}^{-1}$ and $\theta_B = 86.4318°$. The curve was calculated using the XOP program. [83]

where k is the length of the vacuum wave vector, $\Gamma = r_e\lambda^2/(V\pi)$, $F_{0/H}$ is the structure factor and P is the polarization factor, 1 or $\cos 2\theta$ for σ- and π-polarization, respectively. [22] The structure factors and wave vectors are allowed to have imaginary parts to account for attenuation and refraction. Defining the parameters $\xi_{O/H} = (\mathbf{K}_{O/H} \cdot \mathbf{K}_{O/H})^{1/2}k(1 - \Gamma F_0/2)$, the solution to Eq. 14 is written as $\xi_0\xi_H = 1/4k^2P^2\Gamma^2F_HF_{\bar{H}}$. It represents the dispersion surface, i.e. two hyperbolic sheets usually denoted as α- and β-branches (see Fig. 3). Points on these surfaces are called tie points. In the case of parallel beams, the tie point corresponding to the excited reflection is determined by the exact incidence conditions at the vacuum crystal interface. The diameter of the hyperbola determines the Darwin (angular) width of the total reflection regime as depicted in the so-called rocking curve in Fig. 4

$$D = k\Gamma|F_H||P|\sec\theta_B. \tag{15}$$

The corresponding energy bandpass is to first approximation

$$\Delta E = DE\cot\theta_B. \tag{16}$$

The angular acceptance is maximized at backscattering, which is one reason why such geometry is often used in high resolution X-ray spectroscopy. [84] Similarly it is observed that low-index reflections are preferred for a large integrated reflectivity. The amplitude ratio of the waves is expressed as

$$\frac{E_H}{E_O} = -\frac{2\xi_0}{kP\Gamma F_{\bar{H}}} = -\frac{kP\Gamma F_H}{2\xi_H}, \tag{17}$$

from which it is observed that the ratio depends on the deviation from the exact Bragg angle via the ξ parameters. The field intensity inside the crystal within the total

reflection condition is given by

$$I(\mathbf{r}) = |\mathbf{E}_O|^2 \left[1 + \frac{|\mathbf{E}_H|^2}{|\mathbf{E}_O|^2} + 2\frac{|\mathbf{E}_H|}{|\mathbf{E}_O|} \right] \cos\left(\mathbf{H} \cdot \mathbf{r} + \alpha\right), \tag{18}$$

where α is the phase ratio of E_H and E_O, which also is dependent on the deviation from the exact Bragg angle. [80] The wave field forms a standing wave in the region where the incident and diffracted waves overlap. The standing wave is along $\mathbf{H}$ and has the periodicity of the corresponding diffracting planes. The spatial structure of the wave field, and it's manipulation by changing the incidence angle, under the total reflection condition are the basis of X-ray standing wave techniques, which are widely used methods for structural and elemental analysis, and more detailed spectroscopic studies. [80]

The wavefield structure in the Laue case also gives rise to the Borrmann effect, also known as anomalous transmission of X-rays. [22] The Borrmann effect is observed in high quality (i.e. "perfect") crystals and only for π-polarization. For a suitable crystal structure and choice of reflection, the nodes of the wave field can be positioned on heavily absorbing atoms in the lattice. This minimizes absorption by dipole transitions which depend on the field amplitude. Simultaneously the electric quadrupole transitions driven by the field gradient are maximized. The Borrmann effect has recently been demonstrated to yield relative enhancement of E2 absorption in XAS. [85] The enhancement is at most a modest factor of 2 and the dipole suppression modifies the transmitted intensity by a much larger factor. [86] In this thesis, the Borrmann effect is utilized to demonstrate a large enhancement of an E2-absorption-initiated RXES process in paper III.

3 Experimental methods

Synchrotron radiation is essential for X-ray scattering and spectroscopy. The advantages of synchrotron radiation over e.g. X-ray tubes are high brilliance, energy tunability and the ability to produce polarized radiation. The necessary instrumentation starting from the source and ending at the spectrometer is briefly reviewed here. Descriptions of experiments and beamline details follow.

3.1 Properties and production of synchrotron radiation

A relativistic electron beam travelling in a magnetic field experiences the Lorentz force $\mathbf{F} = -e(\mathbf{v} \times \mathbf{B})$ and the path is bent accordingly. The accelerating motion of the electrons results in emission of radiation (Fig. 5). In a laboratory frame, it is observed that the relativistic Doppler effect results in a blueshift, and X-rays are emitted for a properly chosen electron velocity and magnetic field strength. The emitted radiation is focused to a cone in the beam propagation direction with an angular spread of approximately $1/\gamma = (1 - v^2/c^2)^{1/2}$. This intrinsic collimation of synchrotron radiation is a very useful feature for practical implementations of experimental stations. If $\mathbf{B} \parallel \mathbf{z}$, the electron oscillation is in the xy-plane and linearly polarized radiation is observed in the orbit plane of the electron beam (i.e. the xy-plane). In this work, linear polarization was used in all experiments, and the scattered nor emitted photon polarization states were not analysed.

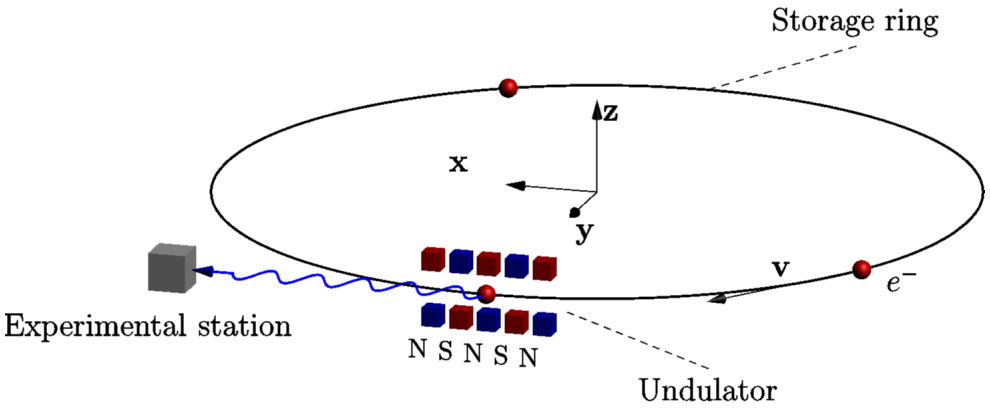

Figure 5: Depiction of a synchrotron. The circulating electron bunch emits intense forward-focused radiation when travelling through a periodic magnetic structure. Optical elements (presented in Fig. 6) are used to produce the desired incident-beam qualities and to direct the beam into an experimental station.

The magnetic structures used for generating X-ray beams are called bending magnets, wigglers and undulators. A bending magnet is a single dipole magnet and radiation is emitted into a relatively broad solid angle that is determined by the elec-

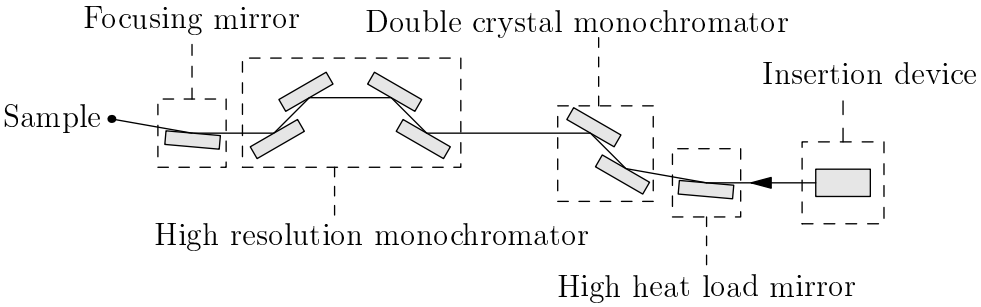

Figure 6: A schematic representation of a spectroscopy beamline layout. The beam propagation direction is indicated by the arrow following the insertion device.

tron deflection in the magnetic field. An array of adjacent dipole magnets with alternating polarities is called a wiggler. The emitted spectrum of bending magnets and wigglers is broad, continuous and is characterized by a critical energy $E_c(\mathrm{keV}) \approx 0.665{E_b}^2(\mathrm{GeV})B(\mathrm{T})$, where E_b is the electron beam energy. Beyond E_c the emitted flux begins to decay rapidly. [87] Wigglers are often used for production of short-wavelength X-rays as high-field magnets are used, increasing the critical energy. A N-pole wiggler produces N deflections of the electron beam and the flux is increased by a factor proportional to N in comparison with a bending magnet. An undulator also consists of an array of alternating multipole magnets. The magnetic fields used are smaller than in wigglers, which results in electron oscillations of smaller amplitude and thus significantly increases the brilliance with a factor proportional to N^2 due to small source size in comparison with a wiggler, and constructive interference of the emitted radiation. [87]

3.2 X-ray monochromators and mirrors

Fig. 6 represents a typical optical layout of a crystal-optics-based hard-X-ray beamline. Following the figure from the insertion device along the beam propagation direction, the first optical element is a high-heat-load mirror designed to suppress unwanted radiation from an undulator and to steer the beam. The mirrors are usually bendable (large) substrates with a thin metal coating on the reflecting side. The mirror typically operates under total-reflection or grazing-incidence conditions, and the focal spot position and size can be altered by adjusting the mirror. The beam then propagates towards a so-called pre-monochromator, here depicted by a double-crystal monochromator. [9,87] The wavelength of the reflected light is chosen by rotating the crystals in accordance with Bragg's law. Monochromators are typically fabricated from very high quality single crystal silicon. The pre-monochromator provides a narrow band pass beam (e.g. 1 eV for Si(111) at 8 keV) that can be used in low resolution experiments. Post-monochromators are used for further narrowing the bandwidth if necessary. In

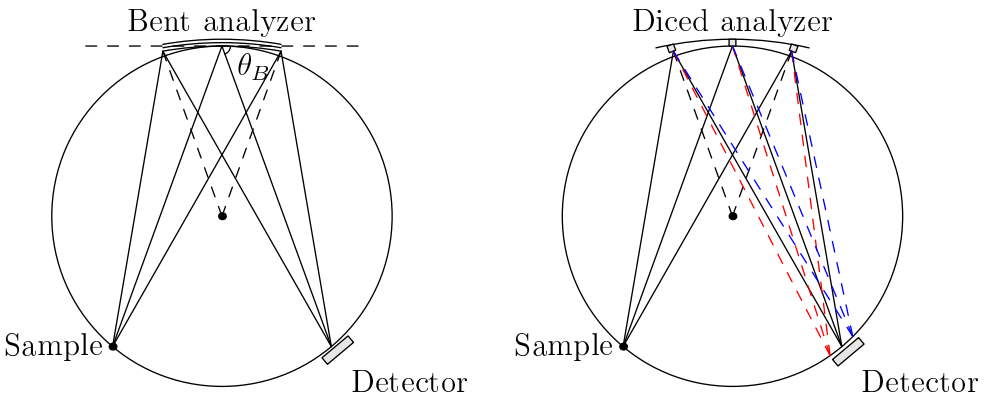

Figure 7: The Rowland circle. The analyzer crystal and detector are placed on a circle of radius R. Their relative position is determined by the analyzer Bragg angle. The analyzer is on a substrate with bending radius of 2R. On the left: The bent analyzer case with point-to-point focusing. On the right: The diced analyzer case, where a finite bandwidth is reflected and dispersed by each dice. The blue and red dashed lines correspond to X-rays which are blue and redshifted with respect to the nominal reflected energy E_B.

Fig. 6 the postmonochromator is represented with a four-bounce monochromator where the beam is diffracted 4 times. [9]

3.3 Crystal analyzer spectrometers

Energy analysis of x-rays with $\Delta E < 1$ eV is a challenging task. Energy-dispersive spectroscopy of keV scale photons has reached a resolution of a few eV in novel superconducting detectors. Traditional semiconductor and scintillation detectors fall several orders of magnitude below the requirements. Wavelength dispersive spectrometers on the other hand readily reach 1 eV resolution, and in very high resolution setups the order of 100 μeV has been achieved. [88] However, the improvement in resolution is often accompanied by a significant loss in spectrometer efficiency. For example, utilizing a high-index reflection does provide a narrow bandpass, but the integrated reflectivity is simultaneously reduced by the narrower angular acceptance in comparison with a low-index case.

Wavelenght-dispersive X-ray spectrometers are often constructed using the Rowland circle concept. The sample, analyzer crystal and radiation detector are positioned on an circle of radius R. [9] (Fig. 7). For a point-like analyzer, this would correspond to selecting a bandwidth determined by the Darwin width from the scattered radiation and diffracting it onto a direction determined by the Bragg angle. For a bent analyzer with crystal bending radius of 2R, the configuration is called the Johann geometry, which provides approximate point-to-point focusing. The analyzer may be constructed

by attaching a silicon wafer on a spherical substrate resulting in a spherically bent analyzer. These are suitable for low to moderate resolution work ($\Delta E \approx 0.3$–1 eV). The bending introduces strains fields that increase the angular acceptance and bandpass, thus actually resulting in a favourable situation for low resolution experiments. A second common option is to attach $\approx 10^4$ small unstrained single crystals to a spherical substrate resulting in a so-called diced spherical analyzer. These are often used when high resolution in the meV regime is sought after. As the crystallites are flat, photons of different energies are reflected into different angles in accordance with Bragg's law. This dispersive effect can be exploited for improving the resolution. The scattered radiation can be analyzed in a position sensitive mode by using a 2D or strip detector (Blue and red dashed lines in Fig. 7). [89, 90]

3.4 Experimental facilities

The experimental results presented in this thesis have been obtained utilizing the 3rd generation synchrotron facilities European Synchrotron Radiation Facility (ESRF) in Grenoble, France. and Advanced Photon Source (APS) in Lemont, Illinois, USA. The electron beam energies at the ESRF and APS are 6 and 7 GeV, respectively.

3.4.1 Beamline ID15-B of the ESRF

The experimental results of Paper II were obtained at the experimental station B of the beamline ID15 of the ESRF. The beamline has a wiggler source providing high energy X-rays. The beamline has a double bent Si(511) monochromator in the Laue geometry. The incident photon energy was 87 keV monochromatized to 0.1% bandwidth. The spectrum of the scattered photons was measured using a 12-element Ge solid state detector placed at a mean scattering angle of 154° and the sample temperature was controlled using a N_2 gas blower provided by the ESRF equipment pool.

3.4.2 Beamline ID20 of the ESRF

The experimental data for papers IV and III were obtained by using the beamline ID20 of the ESRF. ID20 is an undulator beamline with 4 consecutive undulators that provide very brilliant beam for IXS and RXES experiments. [91] The undulators are followed by a high-heat-load mirror which directs the beam to a Si(111) double crystal monochromator. A selection of postmonochromators are available to provide bandpasses even below 25 meV. The postmonochromator is followed by focusing Kirkpatrick-Baez mirror that provides a beam dimension of $\Delta x \approx 10$ μm on the sample. The spectrum of the scattered radiation is resolved using a five-crystal spectrometer in the Johann geometry. Several bent and diced spherical analyzers are available for variable resolution and access to common operating conditions for RXES. In the experiments performed

at ID20 and presented here, diced Si(511) and bent Si(111) analyzers were utilized. The analyzer crystals are hosted in a He filled chamber.

The photons diffracted by the analyzer were counted using a 2D Timepix detector or avalanche photodiodes for papers IV and III, respectively. The 2D detector offers significant experimental advantages. It allows for using a software slit reducing background from e.g. air scattering or sample environment. Practice has shown that in a carefully planned experiment the dominant external noise contribution to experimental data comes from cosmic ray events. The intrinsic noise of the Timepix may be reduced with an electronic threshold mechanism, but this also limits the optimum operational photon energy range to above 7 keV.

3.4.3 Beamline 20-ID-C of the APS

The beamline 20-ID-C of the APS is an undulator beamline designed for IXS and X-ray spectroscopy. Si(111) and Si(311) double crystal setups are available for monochromators. The monochromatic beam is focused using either a toroidal mirror or a Kirkpatric-Baez setup. The scattered radiation was analyzed with the LERIX spectrometer using 18 Si(111) crystals operating at fixed scattering angle in the vertical plane. [92] The photons are counted with 18 scintillator detectors. The sample and the paths from it to the analyzers are in He filled chambers.

4 Results and summary of papers

In this section the motivations, methods and results of papers I-IV are presented.

4.1 Electron momentum density across the metal-insulator transition of VO_2 studied by Compton scattering

The connection with the second moment of Compton profile to the kinetic energy (Eq. 12) has not been widely utilized as of yet, but it presents intriguing possibilities by providing access to thermodynamic quantities such as configurational enthalpies. [73, 74] Similarly, the sensitivity of the Compton profile to the underlying momentum space wave function is useful in studying phase transitions in detail. [93–97]

The MIT of VO_2 has been studied for decades, and VO_2 is a prototype oxide for studies of phase transitions, electronic correlations and electron-phonon coupling. The physical origin of the MIT is still an active topic of study due to the theoretical complexity of treating the electron correlation and phonon-coupling effects on an equal footing. [3] In pristine samples the MIT takes place at approximately 67 °C and is accompanied by a structural phase transition from a insulating monoclinic (M1) phase to a tetragonal metallic rutile phase (R). [16, 98] A phonon mode has been shown to soften when approaching the phase transition from the high temperature R phase, which can be interpreted in favor of a lattice-driven MIT mechanism. [99, 100] Spectroscopic experiments have displayed the relevance of electron correlations in producing the low temperature insulating behavior and the magnitude of the observed band gap. [101–103] The basic electronic structure and excitation spectra have been studied using e.g. advanced density-functional methods, many-body theory, and DMFT. The general observation to be made from these studies is that inclusion of correlation effects beyond the LDA is required to give satisfactory accounts of e.g. photoemission, X-ray and optical absorption and electron energy loss spectra, and to yield correct energy ordering between the phases. [104–109] Here VO_2 was chosen as a test case due to its MITs fundamental and applied relevance, and due to the low number of "non-participator" electrons across the phase boundary with the aims of observing the phase transition in a powder averaged Compton profile, which would translate into progress towards thermodynamic experiments in complex solids with Compton scattering.

Commercial VO_2 powder (99% purity) was obtained from Alpha Aesar and pressed into 3 mm thick pellets. The beamline ID15 of the ESRF was used for this experiment. We used a N_2 gas blower to induce the phase transition in the sample. The phase transition was verified using X-ray diffraction. A CCD detector was placed behind the sample and transmission diffraction patterns were recorded *in situ*. The obtained diffraction patterns compared well with computed patters based on literature references. [16, 98] From the temperature dependence of the patterns we deduced that the

illuminated volume of the sample fully changes phase. We also verified the absence of impurity elements by X-ray fluorescence measurements. The total momentum resolution was calculated to be approximately 0.7 a.u. The processed experimental data was normalized to the expected electron count between ± 10 a.u., calculated using atomic Hartree-Fock Compton profiles. [110] The normalized profiles were aligned by minimizing the difference profile asymmetry, and subtracted to yield the final powder-averaged Compton profile difference across the MIT.

The experimental Compton profile difference exhibits a slight accumulation of momentum density between ± 1.5 a. u. and depleted density between ± 1.5–2 a. u. We then turned to first-principles calculations to investigate whether we could understand the observed behaviour in terms of the metallization or the structural phase transition. The electron momentum densities for the metallic and insulating phase were then calculated using the ELK code. [69] We used experimental atomic geometries in the calculations. [16, 98] For V_{xc} we used the LDA for the R phase and the LDA+U ($U_{\text{eff}} = U - J$, with U=4 eV and J=0.68 eV following Refs. [104, 111], where J is the exchange constant for two electrons in the same d electron state for the M1 phase, to simulate the opening of the energy gap. The spherically averaged electron momentum density was obtained by calculating individual directional Compton profiles with momentum transfer directions spanning the irreducible wedge of the R and M1 Brillouin zones, and calculating their weighted average. The weighting factors were obtained by a numerical Voronoi division of the irreducible Brillouin zones.

The LDA/LDA+U model predicts the positions of the momentum density differences correctly, but the magnitude of the difference is larger by a factor of five than in the experiment. To understand the origin of the discrepancy on a qualitative level, we considered the effects of a) electron correlation, b) density change across the phase transition, and c) local atomic geometries, i.e. bond lengths and thermal motion. Based on existing literature, the order of magnitude difference that hypothesis and b) could produce were found to be too small to explain the observed difference. [112–119]

The combined effects of hypotheses a) and c) on the other hand are supported by prior work. For example, it has been demonstrated that a bond length change of 20% in a LiO dimer can reverse the difference profile. [113] A previous Compton spectroscopy study on water-ethanol mixtures demonstrated that the Compton profile is sensitive bond length differences of 0.003 Å. [120] The uncertainties of the reported atomic positions are of the order 0.001 Å. [16,98] The V atoms in the R phase undergo oscillations with large amplitudes (order of magnitude 0.01 Å). [16] This suggests that the thermal motion of the V atoms might not be well captured by our calculations that use a static approximation for the lattice. Electron correlation effects are particularly relevant for the M1 phase. Both of these effects may cause Compton profiles that are narrower than in experiment, which may lead to overestimation of oscillations in the difference Compton profile. The role of local magnetic moments on the V sites in the

M1 phase and their ordering is also an aspect of the electron correlation problem, and a part of the challenge in finding the true DFT ground state for both phases. [121] Different types of magnetic ground states for the M1 phase were calculated, and we found that the resulting R-M1 difference Compton profiles are sensitive to the presence and ordering of local moments.

We finally suggested that the magnitude error originates mostly from the neglect of thermal motion and correlation effects beyond our LDA/LDA+U model. Further computational and experimental work will be useful for understanding the observed differences, and may give further contribution to the ongoing discussion on the physical origin of the phase transition. The present experiment also suggests that relatively modest improvement of the experimental procedure could produce data with sufficient statistical accuracy for the application of Eq. 12 in the study of thermodynamics of phase transitions in oxides.

4.2 Valence-electron excitations in thin heterostructure samples studied by inelastic x-ray scattering

Studies of electronic excitations in thin films and heterostructures has traditionally been the domain of electron energy loss and optical spectroscopies. There has been considerable interest in various types of TMO films and heterostructures of e.g. high T_c superconductors and ferroelectrics. Following recent demonstrations of total reflection IXS experiments in thin films studying core excitations [122], we set out to study the valence excitation spectrum of the recently discovered $LaAlO_3/SrTiO_3$ heterostructures. The LAO/STO interface exhibits a metal-insulator transition upon deposition of 5 unit cells of LAO on TiO_2 terminated (100) surface of STO. The samples were 55 nm thick and had a layer structure of 1 unit cell LAO/1 unit cell STO and 5 unit cells LAO/5 unit cells STO unit cells, and had been grown with pulsed laser deposition onto a TiO_2 terminated $SrTiO_3$ substrate. [123] Bulk LAO and STO are good electrical insulators with band gaps of 3.2 and 5.6 eV, respectively. Thus the interface metal-insulator transition was seen as a surprising phenomenon. The conducting quasi-2D electron gas has high mobility, and its density depends strongly on the details of the sample preparation. An electrostatic mechanism was put forth to explain the MIT. [17] Subsequent investigations discovered ferromagnetic ordering and superconductivity at the interface at cryogenic temperatures, which demonstrate why oxide interfaces are a popular topic of study: phenomena not found in the bulk can be realized at interfaces. [124]

We performed the experiment using the LERIX spectrometer at the beamline ID20-C of the APS. LAO/STO heterostructures and bulk references of LAO and STO with (001) surfaces were investigated in the valence and shallow core excitation regimes. The surface sensitivity of the experiment was verified by using a post sample fluorescent screen, on which we could visually observe the beam reflected off the sample surface

when the samples were brought to the beam at low glancing angles below 0.5°.

We determined that approximately half of the IXS signal originates from the heterostructure, thus proving that the valence $S(\mathbf{q}, \omega)$ of thin samples is measurable. Somewhat surprisingly, we found that the excitation spectra is not modified appreciably even in heterostructures with 1/1 stacking, where one could naively expect to observe broadening or shifts in the interband and semicore peaks. A recent study probing the reflectivity of LAO/STO films up to 30 eV displayed substantial changes upon STO deposition in the energy range of 15–20 eV. [125] Further experimental work would be required to deduce what causes the apparent stability of $S(\mathbf{q}, \omega)$ in the heterostructure samples.

For analysis of the spectral features we performed free-ion multiplet and RPA calculations for bulk LAO and STO. We identified the natures of the observed peaks according to the behavior of the dielectric function at the peak energies and by comparison with the multiplet model. The comparison with RPA calculations was made for a single momentum transfer of (0.5,0,0.08) $|a^*|$, where $|a^*|$ is the appropriate reciprocal lattice vector length for STO or LAO. The experimental high energy low-q $S(\mathbf{q}, \omega)$ for STO exhibits an interband peak at 14 eV and a damped volume plasmon below 30 eV, with $\mathrm{Im}\,\epsilon > 0.5$ at the minimum of Re, which has no true zero crossing that would signify a well defined plasmon excitation. For LAO the $S(\mathbf{q}, \omega)$ is very similar. An interband peak is observed at 13 eV and the plasma resonance at 30 eV is again damped by a finite $\mathrm{Im}\,\epsilon$ and there are no zero crossings of $\mathrm{Re}\,\epsilon$. Our main result, the demonstration of the measurability of $S(\mathbf{q}, \omega)$ in a thin layer system is an interesting result. This may lead to quite intriguing applications such as e.g. measuring dipole forbidden excitations in thin films.

4.3 The Borrmann effect and resonant x-ray emission spectroscopy

RXES is a commonly used method in electronic structure research and has been crucial in e.g. elucidating the nature of magnetism in REOs. [77, 78] Intra unit cell spatial sensitivity, i.e. site selectivity, in RIXS can ne achieved by exploiting the differences in the X-ray absorption resonance energy on atomic sites with differing chemical environments. A second route towards spatial sensitivity in X-ray spectroscopy has been to exploit standing wave effects in dynamical X-ray diffraction to manipulate the X-ray wavefield inside a sample (Eq. 18). [80, 81] The utilisation of standing wave effects in high resolution photon-in photon-out spectroscopy can be considered to be in its infancy. Experiments of this kind are challenging as on one hand high-resolution experiments on weak signals such as RXES necessarily require a high incident monochromatic flux with a small beam footprint on the sample, and a low bandpass analyzer. On the other hand, to utilize standing wave methods efficiently, the incident beam divergence

should at maximum correspond to the Darwin width of the relevant reflection. Collimating optics however enlargen the beam footprint and may deteriorate the energy resolution.

Following the successful demonstrations of utilizing the Borrmann effect in X-ray absorption [85, 86] to reveal quadrupolar absorption channels at the Gd L absorption edges in GGG and Ti K edge in STO, we chose to investigate how the observed effect would manifest itself in the RXES cross section. We used GGG as the sample and investigated the RXES spectrum at the Gd L_3 edge. Investigations of standing wave RXES are interesting from several perspectives. For example, RXES has previously been utilized to obtain proof for quadrupole excitations at the rare earth L absorption edges in several REOs. [77, 78] The magnetic properties of RE containing solids have been studied utilizing X-ray magnetic dichroism spectroscopies, which within certain approximations yield access to the ground state expectation values of the spin and angular momentum operators of the studied ion. [75, 76, 79] These quantities are accessed via magneto-optical sum rules, and the analysis depends on the multipolarity of the electronic transition involved. The dipole and quadrupole signals have distinct angular dependencies, which can be utilized for identification of the multipolarity. However, for certain electronic states such as the $^{7/2}S_{1/2}$ state of the Gd^{3+} ion, the quadrupole absorption has an angular dependence very similar to the dipole case. [77] Another important motivation for this work is the aforementioned fact (as the equation (18) implies) that the standing wave structure and its manipulation might yield access to intra unit cell spatial sensitivity, as already has been demonstrated in previous works investigating the photoelectron or X-ray fluorescence yield (with low energy resolution) under the diffraction condition. [80, 81]

The experiment reported in paper III was performed at beamline ID20 of the ESRF. The sample was a commercial GGG substrate crystal obtained from Pi Kem LTD. We used the (008) reflection of the GGG crystal to set up the standing wave field. Then we optimized the beam divergence by maximizing the intensity of the anomalously transmitted beam. The Bragg angles were given by the incident photon energies spanning the studied Gd L_3 absorption edge. We verified that the Borrmann effect takes place by measuring the diffracted and transmitted beams. We investigated the 2p-4f/5d excitation channel with 3d-2p de-excitation, i.e. the L_α emission. The emitted Gd Lα radiation was analyzed using 3 spherically bent Si(333) analyzer crystals and the scattered photons were counted with avalanche photodiodes. We performed the measurement on and off the diffraction condition from the entrance and exit surfaces of the sample. The β-branch is absorbed near the entrance surface and gives rise to normal-RXES. The anomalously transmitted α-branch produces a new source for the RXES process to occur, with modified dipole and quadrupole absorption in the initial to intermediate state transition. We observed the RXES spectrum from the exit surface the spectra displayed an impressive approximately 5-fold relative enhancement of

decay events from E2-allowed intermediate states.

4.4 Plasmons in TMDCs studied with inelastic X-ray scattering

Transition-metal dichalcogenides exhibit quasi-2D electronic structures. Many TMDC compounds exhibit charge-density-wave transitions at low temperature (T<100 K) and a superconducting transition below 10 K. [20] The crystal structures of TMDCs are hexagonal and in analogy with graphite can be grown in polytypes differentiated by the stacking sequence of planar hexagonal layers. Our work aimed at investigating the plasmon excitations in two TMDCs, 2H-$NbSe_2$ and 2H-$Cu_{0.2}NbS_2$. In recent years there has been considerable interest in monolayer TMDCs which exhibit a band gap making them potentially useful in e.g. optoelectronic device applications and fundamental studies of 2D electron systems. The optical properties of TMDCs and the applicability of band structure methods and simple non-interacting response functions is thus a question of interest.

The TMDC crystals were studied using beamline ID20 of the ESRF. We used a Si(111) monochromator and diced Si(533) analyzers and the energy and momentum resolutions were approximately 1 eV and 0.1 $Å^{-1}$, respectively. The sample compositions were confirmed with X-ray fluorescence. The samples were aligned with X-ray diffraction and the $S(\mathbf{q},\omega)$ was measured up to energy losses of 50 eV for momentum transfers along the reciprocal lattice vector $\mathbf{c}^*$. The absolute values ranged from Q=2/c* to Q=2.5/c* for $Cu_{0.2}NbS_2$ and Q=1.5/c* to Q=2.5/c* for $NbSe_2$. The measurements were performed at room temperature.

The theoretical analysis of the electronic structure was performed utilizing DFT in the local density approximation. A rigid-band approach was used for simulating the Cu stabilized NbS_2 phase. The gross details of the electronic structures of the studied compounds are very similar, and states in the vicinity of the Fermi level can be interpreted in terms of occupied π and σ bands and an unoccupied π^* band. In the theoretical analysis it was found that inclusion of semicore states and local field effects are crucial for understanding the excitation spectrum. For $NbSe_2$ a RPA calculation with local fields produces an excellent agreement with experiment, whereas for $Cu_{0.2}NbS_2$ the theoretical spectra have decent agreement in shape, but exhibit a blueshift of some few eV. The inclusion of the local field effects and semicore electron in the calculations was required to understand the momentum dependence of the high-energy-plasmon excitation at approximately 25 eV. The plasmon energy initially blueshifts as the momentum transfer is increased, and at large momentum transfers the activation of non-dipolar semicore excitations turns the initial positive slope of the plasmon dispersion to a negative one.

5 Conclusions

Here I will gather the main conclusions of papers I-IV, and present a few more general conclusions and possible future research directions that can be drawn viewing the published results as a whole.

In paper I, we succeeded in demonstrating that the isotropic CP difference across the MIT of VO_2 can be measured. The experimental data in itself could be useful as a reference for validation of theoretical models of the MIT. We also found the results promising for further experiments in attempting to derive thermodynamic quantities in oxide materials from Compton profile differences. The possibility to use a combination of microscopic methods, e.g. Compton scattering and high resolution IXS from phonons or thermal diffuse scattering, to derive values of electronic and lattice specific heats is intriguing. [73, 74, 126] This will be highly useful when a given sample is challenging for traditional transport-property measurements.

The most important finding of paper II was our ability to demonstrate that IXS can be used to study the $S(\mathbf{q}, \omega)$ of thin multilayer samples. As IXS can access momentum transfers challenging to electron energy loss spectroscopy, and provides a straightforward comparison with theoretical response functions in contrast with soft X-ray RIXS, there are numerous interesting applications of IXS in e.g. thin films and heterostructures of TMOs. The computational part of the work allowed us to identify the various observed excitations and are in line with previous literature highlighting the importance of local field effects and semicore states in the dielectric function. [56]

In paper III we demonstrated a novel application of the Borrmann effect to RXES. Our successful demonstration of large effects in the RXES by manipulating the absorption transition rate enables simple identification of E2-transitions at room temperature. There are several exciting possibilities in utilizing the Borrmann effect that are yet to be investigated. Further experiments and theoretical studies should be pursued to investigate where our findings might find useful applications.

In paper IV the good agreement between experiment and theoretical calculations allowed us to interpret the high-frequency plasmon behavior in TMDCs within a simple scheme combining DFT and RPA calculations. The level of agreement suggests that relatively low level electronic structure theory can be utilized in predicting the optical properties of TMDCs. Further experiments should be undertaken to see whether this conclusion holds for smaller ω than what our experiment probed.

In summary, the results of papers I-III demonstrate that current experimental facilities for IXS have reached a level of performance that facilitates the following: i) studies of electronic excitations in film like samples, ii) revealing a MIT signature in a powdered oxide sample, iii) utilization of X-ray standing wave effects in high resolution spectroscopy. Furthermore, paper IV demonstrates well how combining IXS experiments with first principles calculations yields detailed insight on the electronic

excitation spectra in TMDCs.

References

[1] A. L. Fetter and J. D. Walecka, *Quantum theory of many-particle systems* (McGraw-Hill, 1971).

[2] G. Mahan, *Many body physics* (Plenum press, 1981).

[3] M. Imada, A. Fujimori, and Y. Tokura, *Metal-insulator transitions*, Reviews of Modern Physics **70**, 1039 (1998).

[4] R. M. Martin, *Electronic structure: basic theory and practical methods* (Cambridge university press, 2004).

[5] P. P. Ewald, 50 years of X-Ray Diffraction, http://www.iucr.org/iucr-top/publ/50YearsOfXrayDiffraction/index.html.

[6] A. H. Compton, *A Quantum Theory of the Scattering of X-rays by Light Elements*, Phys. Rev. **21**, 483 (1923).

[7] M. Cooper, P. Mijnarends, N. Shiotani, N. Sakai, and A. Bansil, *X-ray Compton scattering* (OUP Oxford, 2004).

[8] B. Mattern, G. Seidler, M. Haave, J. Pacold, R. Gordon, J. Planillo, J. Quintana, and B. Rusthoven, *A plastic miniature x-ray emission spectrometer based on the cylindrical von Hamos geometry*, Review of Scientific Instruments **83**, 023901 (2012).

[9] W. Schülke, *Electron dynamics by inelastic X-ray scattering* (OUP Oxford, 2007).

[10] K. Hämäläinen, D. P. Siddons, J. B. Hastings, and L. E. Berman, *Elimination of the inner-shell lifetime broadening in x-ray-absorption spectroscopy*, Phys. Rev. Lett. **67**, 2850 (1991).

[11] K. Hämäläinen, C.-C. Kao, J. B. Hastings, D. P. Siddons, L. E. Berman, V. Stojanoff, and S. P. Cramer, *Spin-dependent x-ray absorption of MnO and* MnF_2, Phys. Rev. B **46**, 14274 (1992).

[12] F. De Groot and A. Kotani, *Core level spectroscopy of solids* (CRC press, 2008).

[13] F. J. Morin, *Oxides Which Show a Metal-to-Insulator Transition at the Neel Temperature*, Phys. Rev. Lett. **3**, 34 (1959).

[14] J. Hubbard, *Electron Correlations in Narrow Energy Bands*, Proceedings of the Royal Society of London A: Mathematical, Physical and Engineering Sciences **276**, 238 (1963).

[15] N. Mott, *Metal-insulator transition*, Reviews of Modern Physics **40**, 677 (1968).

[16] D. B. McWhan, M. Marezio, J. P. Remeika, and P. D. Dernier, *X-ray diffraction study of metallic* VO_2, Phys. Rev. B **10**, 490 (1974).

[17] A. Ohtomo and H. Hwang, *A high-mobility electron gas at the $LaAlO_3/SrTiO_3$ heterointerface*, Nature **427**, 423 (2004).

[18] J. A. Paddison, H. Jacobsen, O. A. Petrenko, M. T. Fernández-Díaz, P. P. Deen, and A. L. Goodwin, *Hidden order in spin-liquid $Gd_3Ga_5O_{12}$*, Science **350**, 179 (2015).

[19] Q. H. Wang, K. Kalantar-Zadeh, A. Kis, J. N. Coleman, and M. S. Strano, *Electronics and optoelectronics of two-dimensional transition metal dichalcogenides*, Nature nanotechnology **7**, 699 (2012).

[20] A. H. Castro Neto, *Charge Density Wave, Superconductivity, and Anomalous Metallic Behavior in 2D Transition Metal Dichalcogenides*, Phys. Rev. Lett. **86**, 4382 (2001).

[21] A. Kuc, N. Zibouche, and T. Heine, *Influence of quantum confinement on the electronic structure of the transition metal sulfide TS_2*, Phys. Rev. B **83**, 245213 (2011).

[22] B. W. Batterman and H. Cole, *Dynamical Diffraction of X Rays by Perfect Crystals*, Rev. Mod. Phys. **36**, 681 (1964).

[23] G. Giuliani and G. Vignale, *Quantum theory of the electron liquid* (Cambridge university press, 2005).

[24] P. Hohenberg and W. Kohn, *Inhomogeneous Electron Gas*, Phys. Rev. **136**, B864 (1964).

[25] W. Kohn and L. J. Sham, *Self-Consistent Equations Including Exchange and Correlation Effects*, Phys. Rev. **140**, A1133 (1965).

[26] S. Goedecker, M. Teter, and J. Hutter, *Separable dual-space Gaussian pseudopotentials*, Phys. Rev. B **54**, 1703 (1996).

[27] J. P. Perdew, K. Burke, and M. Ernzerhof, *Generalized Gradient Approximation Made Simple*, Phys. Rev. Lett. **77**, 3865 (1996).

[28] D. M. Ceperley and B. J. Alder, *Ground State of the Electron Gas by a Stochastic Method*, Phys. Rev. Lett. **45**, 566 (1980).

[29] V. I. Anisimov, F. Aryasetiawan, and A. I. Lichtenstein, *First-principles calculations of the electronic structure and spectra of strongly correlated systems: the LDA + U method*, Journal of Physics: Condensed Matter **9**, 767 (1997).

[30] N. W. Ashcroft and N. D. Mermin, *Solid state physics*, Saunders, Philadelphia 293 (1976).

[31] The Abinit code, http://www.abinit.org.

[32] N. Troullier and J. L. Martins, *Efficient pseudopotentials for plane-wave calculations*, Phys. Rev. B **43**, 1993 (1991).

[33] C. Hartwigsen, S. Goedecker, and J. Hutter, *Relativistic separable dual-space Gaussian pseudopotentials from H to Rn*, Phys. Rev. B **58**, 3641 (1998).

[34] C. L. Reis, J. Pacheco, and J. L. Martins, *First-principles norm-conserving pseudopotential with explicit incorporation of semicore states*, Physical Review B **68**, 155111 (2003).

[35] J. C. Slater, *An Augmented Plane Wave Method for the Periodic Potential Problem*, Phys. Rev. **92**, 603 (1953).

[36] The Elk code, http://elk.sourceforge.net.

[37] H. J. F. Jansen and A. J. Freeman, *Total-energy full-potential linearized augmented-plane-wave method for bulk solids: Electronic and structural properties of tungsten*, Phys. Rev. B **30**, 561 (1984).

[38] A. Seidl, A. Görling, P. Vogl, J. A. Majewski, and M. Levy, *Generalized Kohn-Sham schemes and the band-gap problem*, Phys. Rev. B **53**, 3764 (1996).

[39] L. Hedin, *New Method for Calculating the One-Particle Green's Function with Application to the Electron-Gas Problem*, Phys. Rev. **139**, A796 (1965).

[40] F. Aryasetiawan and O. Gunnarsson, *The GW method*, Reports on Progress in Physics **61**, 237 (1998).

[41] G. Onida, L. Reining, and A. Rubio, *Electronic excitations: density-functional versus many-body Green's-function approaches*, Rev. Mod. Phys. **74**, 601 (2002).

[42] F. Bruneval, N. Vast, and L. Reining, *Effect of self-consistency on quasiparticles in solids*, Phys. Rev. B **74**, 045102 (2006).

[43] A. Georges, G. Kotliar, W. Krauth, and M. J. Rozenberg, *Dynamical mean-field theory of strongly correlated fermion systems and the limit of infinite dimensions*, Rev. Mod. Phys. **68**, 13 (1996).

[44] R. Chitra and G. Kotliar, *Effect of Long Range Coulomb Interactions on the Mott Transition*, Phys. Rev. Lett. **84**, 3678 (2000).

[45] M. Blume, *Magnetic scattering of x rays*, Journal of Applied Physics **57**, 3615 (1985).

[46] J. H. McGuire, *Electron correlation dynamics in atomic collisions* (Cambridge University Press, 1997).

[47] A. Kotani and S. Shin, *Resonant inelastic x-ray scattering spectra for electrons in solids*, Rev. Mod. Phys. **73**, 203 (2001).

[48] B. C. Larson, W. Ku, J. Z. Tischler, C.-C. Lee, O. D. Restrepo, A. G. Eguiluz, P. Zschack, and K. D. Finkelstein, *Nonresonant Inelastic X-Ray Scattering and Energy-Resolved Wannier Function Investigation of d-d Excitations in NiO and CoO*, Phys. Rev. Lett. **99**, 026401 (2007).

[49] M. W. Haverkort, A. Tanaka, L. H. Tjeng, and G. A. Sawatzky, *Nonresonant Inelastic X-Ray Scattering Involving Excitonic Excitations: The Examples of NiO and CoO*, Phys. Rev. Lett. **99**, 257401 (2007).

[50] N. Hiraoka, M. Suzuki, K. D. Tsuei, H. Ishii, Y. Q. Cai, M. W. Haverkort, C. C. Lee, and W. Ku, *dd excitations in three-dimensional q-space: A nonresonant inelastic X-ray scattering study on NiO*, EPL (Europhysics Letters) **96**, 37007 (2011).

[51] E. Runge and E. K. U. Gross, *Density-Functional Theory for Time-Dependent Systems*, Phys. Rev. Lett. **52**, 997 (1984).

[52] M. Petersilka, U. J. Gossmann, and E. K. U. Gross, *Excitation Energies from Time-Dependent Density-Functional Theory*, Phys. Rev. Lett. **76**, 1212 (1996).

[53] S. G. Louie, J. R. Chelikowsky, and M. L. Cohen, *Local-Field Effects in the Optical Spectrum of Silicon*, Phys. Rev. Lett. **34**, 155 (1975).

[54] J. A. Soininen and E. L. Shirley, *Effects of electron-hole interaction on the dynamic structure factor: Application to nonresonant inelastic x-ray scattering*, Phys. Rev. B **61**, 16423 (2000).

[55] I. G. Gurtubay, W. Ku, J. M. Pitarke, A. G. Eguiluz, B. C. Larson, J. Tischler, and P. Zschack, *Large crystal local-field effects in the dynamical structure factor of rutile* TiO_2, Phys. Rev. B **70**, 201201 (2004).

[56] I. G. Gurtubay, J. M. Pitarke, W. Ku, A. G. Eguiluz, B. C. Larson, J. Tischler, P. Zschack, and K. D. Finkelstein, *Electron-hole and plasmon excitations in* 3*d transition metals: Ab initio calculations and inelastic x-ray scattering measurements*, Phys. Rev. B **72**, 125117 (2005).

[57] S. L. Adler, *Quantum Theory of the Dielectric Constant in Real Solids*, Phys. Rev. **126**, 413 (1962).

[58] N. Wiser, *Dielectric Constant with Local Field Effects Included*, Phys. Rev. **129**, 62 (1963).

[59] H.-C. Weissker, J. Serrano, S. Huotari, E. Luppi, M. Cazzaniga, F. Bruneval, F. Sottile, G. Monaco, V. Olevano, and L. Reining, *Dynamic structure factor and dielectric function of silicon for finite momentum transfer: Inelastic x-ray scattering experiments and ab initio calculations*, Phys. Rev. B **81**, 085104 (2010).

[60] M. Cazzaniga, H.-C. Weissker, S. Huotari, T. Pylkkänen, P. Salvestrini, G. Monaco, G. Onida, and L. Reining, *Dynamical response function in sodium and aluminum from time-dependent density-functional theory*, Phys. Rev. B **84**, 075109 (2011).

[61] M. Rohlfing and S. G. Louie, *Electron-Hole Excitations in Semiconductors and Insulators*, Phys. Rev. Lett. **81**, 2312 (1998).

[62] E. L. Shirley, *Ab Initio Inclusion of Electron-Hole Attraction: Application to X-Ray Absorption and Resonant Inelastic X-Ray Scattering*, Phys. Rev. Lett. **80**, 794 (1998).

[63] S. Albrecht, L. Reining, R. Del Sole, and G. Onida, *Ab Initio Calculation of Excitonic Effects in the Optical Spectra of Semiconductors*, Phys. Rev. Lett. **80**, 4510 (1998).

[64] M. Rohlfing and S. G. Louie, *Electron-hole excitations and optical spectra from first principles*, Phys. Rev. B **62**, 4927 (2000).

[65] The YAMBO code, http://www.yambo-code.org.

[66] P. Eisenberger and P. M. Platzman, *Compton Scattering of X Rays from Bound Electrons*, Phys. Rev. A **2**, 415 (1970).

[67] P. Eisenberger and W. A. Reed, *Relationship of the relativistic Compton cross section to the electron's velocity distribution*, Phys. Rev. B **9**, 3237 (1974).

[68] P. Holm, *Relativistic Compton cross section for general central-field Hartree-Fock wave functions*, Phys. Rev. A **37**, 3706 (1988).

[69] D. Ernsting, D. Billington, T. D. Haynes, T. E. Millichamp, J. W. Taylor, J. A. Duffy, S. R. Giblin, J. K. Dewhurst, and S. B. Dugdale, *Calculating electron momentum densities and Compton profiles using the linear tetrahedron method*, Journal of Physics: Condensed Matter **26**, 495501 (2014).

[70] W. Weyrich, P. Pattison, and B. Williams, *Fourier analysis of the Compton profile: atoms and molecules*, Chemical Physics **41**, 271 (1979).

[71] K. Hämäläinen, S. Huotari, J. Laukkanen, A. Soininen, S. Manninen, C.-C. Kao, T. Buslaps, and M. Mezouar, *Free electron gas under high pressure*, Phys. Rev. B **62**, R735 (2000).

[72] S. Huotari, J. A. Soininen, T. Pylkkänen, K. Hämäläinen, A. Issolah, A. Titov, J. McMinis, J. Kim, K. Esler, D. M. Ceperley, M. Holzmann, and V. Olevano, *Momentum Distribution and Renormalization Factor in Sodium and the Electron Gas*, Phys. Rev. Lett. **105**, 086403 (2010).

[73] I. R. Epstein, *Calculation of Atomic and Molecular Momentum Expectation Values and Total Energies from Compton-Scattering Data*, Phys. Rev. A **8**, 160 (1973).

[74] K. Nygård, M. Hakala, S. Manninen, M. Itou, Y. Sakurai, and K. Hämäläinen, *Configurational Energetics in Ice* I*h Probed by Compton Scattering*, Phys. Rev. Lett. **99**, 197401 (2007).

[75] P. Carra and M. Altarelli, *Dichroism in the x-ray absorption spectra of magnetically ordered systems*, Phys. Rev. Lett. **64**, 1286 (1990).

[76] B. T. Thole, P. Carra, F. Sette, and G. van der Laan, *X-ray circular dichroism as a probe of orbital magnetization*, Phys. Rev. Lett. **68**, 1943 (1992).

[77] M. H. Krisch, C. C. Kao, F. Sette, W. A. Caliebe, K. Hämäläinen, and J. B. Hastings, *Evidence for a Quadrupolar Excitation Channel at the L_{III} Edge of Gadolinium by Resonant Inelastic X-Ray Scattering*, Phys. Rev. Lett. **74**, 4931 (1995).

[78] F. Bartolomé, J. M. Tonnerre, L. Sève, D. Raoux, J. Chaboy, L. M. García, M. Krisch, and C. C. Kao, *Identification of Quadrupolar Excitation Channels at the L_3 Edge of Rare-Earth Compounds*, Phys. Rev. Lett. **79**, 3775 (1997).

[79] G. van der Laan, *Magnetic Linear X-Ray Dichroism as a Probe of the Magnetocrystalline Anisotropy*, Phys. Rev. Lett. **82**, 640 (1999).

[80] I. Vartanyants and M. Kovalchuk, *Theory and applications of x-ray standing waves in real crystals*, Reports on Progress in Physics **64**, 1009 (2001).

[81] D. Woodruff, *Surface structure determination using x-ray standing waves*, Reports on Progress in Physics **68**, 743 (2005).

[82] M. Hart, *Bragg reflection x ray optics*, Reports on Progress in Physics **34**, 435 (1971).

[83] The XOP program, http://www.esrf.eu/Instrumentation/software/data-analysis/xop2.4.

[84] A. Caticha and S. Caticha-Ellis, *Dynamical theory of x-ray diffraction at Bragg angles near $\frac{\pi}{2}$*, Phys. Rev. B **25**, 971 (1982).

[85] R. F. Pettifer, S. P. Collins, and D. Laundy, *Quadrupole transitions revealed by Borrmann spectroscopy*, Nature **454**, 196 (2008).

[86] M. Tolkiehn, T. Laurus, and S. P. Collins, *Effects of temperature and anisotropy on quadrupole absorption in Borrmann spectroscopy*, Phys. Rev. B **84**, 241101 (2011).

[87] J. Baruchel, J.-L. Hodeau, M. S. Lehmann, J.-R. Regnard, and C. Schlenker, *Neutron and synchrotron radiation for condensed matter studies* (Springer, 1993).

[88] Y. Shvydko, S. Stoupin, D. Shu, S. P. Collins, K. Mundboth, J. Sutter, and M. Tolkiehn, *High-contrast sub-millivolt inelastic X-ray scattering for nano-and mesoscale science*, Nature communications **5**, (2014).

[89] S. Huotari, G. Vankó, F. Albergamo, C. Ponchut, H. Graafsma, C. Henriquet, R. Verbeni, and G. Monaco, *Improving the performance of high-resolution X-ray spectrometers with position-sensitive pixel detectors*, Journal of synchrotron radiation **12**, 467 (2005).

[90] S. Huotari, F. Albergamo, G. Vankó, R. Verbeni, and G. Monaco, *Resonant inelastic hard x-ray scattering with diced analyzer crystals and position-sensitive detectors*, Review of scientific instruments **77**, 053102 (2006).

[91] M. M. Sala, C. Henriquet, L. Simonelli, R. Verbeni, and G. Monaco, *High energy-resolution set-up for Ir L_3 edge RIXS experiments*, Journal of Electron Spectroscopy and Related Phenomena **188**, 150 (2013).

[92] T. Fister, G. Seidler, L. Wharton, A. Battle, T. Ellis, J. Cross, A. Macrander, W. Elam, T. Tyson, and Q. Qian, *Multielement spectrometer for efficient measurement of the momentum transfer dependence of inelastic X-ray scattering*, Review of scientific instruments **77**, 63901 (2006).

[93] A. Shukla, B. Barbiellini, A. Erb, A. Manuel, T. Buslaps, V. Honkimäki, and P. Suortti, *Hole depletion and localization due to disorder in insulating* $PrBa_2Cu_3O_{7-\delta}$*: A Compton scattering study*, Phys. Rev. B **59**, 12127 (1999).

[94] N. Hiraoka, T. Buslaps, V. Honkimäki, H. Minami, and H. Uwe, *Fermi surface nesting in* $Ba_{1-x}K_xBiO_3$ *observed by Compton profile measurement*, Phys. Rev. B **71**, 205106 (2005).

[95] N. Hiraoka, T. Buslaps, V. Honkimäki, J. Ahmad, and H. Uwe, *Fermi surface nesting in* $Ba_{1-x}K_xBiO_3$ *observed by Compton scattering: Three-dimensional momentum density reconstruction study*, Phys. Rev. B **75**, 121101 (2007).

[96] B. Barbiellini, A. Koizumi, P. E. Mijnarends, W. Al-Sawai, H. Lin, T. Nagao, K. Hirota, M. Itou, Y. Sakurai, and A. Bansil, *Role of Oxygen Electrons in the Metal-Insulator Transition in the Magnetoresistive Oxide* $La_{2-2x}Sr_{1+2x}Mn_2O_7$ *Probed by Compton Scattering*, Phys. Rev. Lett. **102**, 206402 (2009).

[97] Y. Sakurai, M. Itou, B. Barbiellini, P. E. Mijnarends, R. S. Markiewicz, S. Kaprzyk, J.-M. Gillet, S. Wakimoto, M. Fujita, S. Basak, Y. J. Wang, W. Al-Sawai, H. Lin, A. Bansil, and K. Yamada, *Imaging Doped Holes in a Cuprate Superconductor with High-Resolution Compton Scattering*, Science **332**, 698 (2011).

[98] J. M. Longo and P. Kierkegaard, *A Refinement of the Structure of* $V0_2$, Acta Chem. Scand **24**, 4 (1970).

[99] R. Srivastava and L. L. Chase, *Raman Spectrum of Semiconducting and Metallic* VO_2, Phys. Rev. Lett. **27**, 727 (1971).

[100] J. D. Budai, J. Hong, M. E. Manley, E. D. Specht, C. W. Li, J. Z. Tischler, D. L. Abernathy, A. H. Said, B. M. Leu, L. A. Boatner, *et al.*, *Metallization of vanadium dioxide driven by large phonon entropy*, Nature **515**, 535 (2014).

[101] S. Shin, S. Suga, M. Taniguchi, M. Fujisawa, H. Kanzaki, A. Fujimori, H. Daimon, Y. Ueda, K. Kosuge, and S. Kachi, *Vacuum-ultraviolet reflectance and photoemission study of the metal-insulator phase transitions in* VO_2*,* V_6O_{13}*, and* V_2O_3, Phys. Rev. B **41**, 4993 (1990).

[102] R. Eguchi, M. Taguchi, M. Matsunami, K. Horiba, K. Yamamoto, Y. Ishida, A. Chainani, Y. Takata, M. Yabashi, D. Miwa, Y. Nishino, K. Tamasaku, T. Ishikawa, Y. Senba, H. Ohashi, Y. Muraoka, Z. Hiroi, and S. Shin, *Photoemission evidence for a Mott-Hubbard metal-insulator transition in* VO_2, Phys. Rev. B **78**, 075115 (2008).

[103] S. Suga, A. Sekiyama, S. Imada, T. Miyamachi, H. Fujiwara, A. Yamasaki, K. Yoshimura, K. Okada, M. Yabashi, K. Tamasaku, *et al.*, *8 keV photoemission of the metal–insulator transition system VO_2*, New Journal of Physics **11**, 103015 (2009).

[104] S. Biermann, A. Poteryaev, A. I. Lichtenstein, and A. Georges, *Dynamical Singlets and Correlation-Assisted Peierls Transition in* VO_2, Phys. Rev. Lett. **94**, 026404 (2005).

[105] M. Gatti, F. Bruneval, V. Olevano, and L. Reining, *Understanding Correlations in Vanadium Dioxide from First Principles*, Phys. Rev. Lett. **99**, 266402 (2007).

[106] V. Eyert, VO_2*: A Novel View from Band Theory*, Phys. Rev. Lett. **107**, 016401 (2011).

[107] R. Grau-Crespo, H. Wang, and U. Schwingenschlögl, *Why the Heyd-Scuseria-Ernzerhof hybrid functional description of VO_2 phases is not correct*, Phys. Rev. B **86**, 081101 (2012).

[108] F. Iori, M. Gatti, and A. Rubio, *Role of nonlocal exchange in the electronic structure of correlated oxides*, Phys. Rev. B **85**, 115129 (2012).

[109] M. Gatti, G. Panaccione, and L. Reining, *Effects of Low-Energy Excitations on Spectral Properties at Higher Binding Energy: The Metal-Insulator Transition of* VO_2, Phys. Rev. Lett. **114**, 116402 (2015).

[110] F. Biggs, L. Mendelsohn, and J. Mann, *Hartree-Fock Compton profiles for the elements*, Atomic data and nuclear data tables **16**, 201 (1975).

[111] J. M. Tomczak and S. Biermann, *Effective band structure of correlated materials: the case of VO_2*, Journal of Physics: Condensed Matter **19**, 365206 (2007).

[112] J. Lehtola, M. Hakala, J. Vaara, and K. Hämäläinen, *Calculation of isotropic Compton profiles with Gaussian basis sets*, Physical Chemistry Chemical Physics **13**, 5630 (2011).

[113] K. Nygård, M. Hakala, S. Manninen, K. Hämäläinen, M. Itou, A. Andrejczuk, and Y. Sakurai, *Ion hydration studied by x-ray Compton scattering*, Phys. Rev. B **73**, 024208 (2006).

[114] B. Králik, P. Delaney, and S. G. Louie, *Correlation effects in the Compton profile of silicon*, Physical review letters **80**, 4253 (1998).

[115] C. Filippi and D. M. Ceperley, *Quantum Monte Carlo calculation of Compton profiles of solid lithium*, Physical Review B **59**, 7907 (1999).

[116] K. Nygård, S. Huotari, K. Hämäläinen, S. Manninen, T. Buslaps, N. H. Babu, M. Kambara, and D. Cardwell, *Temperature dependence of MgB_2 Compton profiles*, Physical Review B **69**, 020501 (2004).

[117] M. Hakala, K. Nygård, S. Manninen, S. Huotari, T. Buslaps, A. Nilsson, L. Pettersson, and K. Hämäläinen, *Correlation of hydrogen bond lengths and angles in liquid water based on Compton scattering*, The Journal of chemical physics **125**, 084504 (2006).

[118] V. Olevano, A. Titov, M. Ladisa, K. Hämäläinen, S. Huotari, and M. Holzmann, *Momentum distribution and Compton profile by the ab initio GW approximation*, Physical Review B **86**, 195123 (2012).

[119] K. Nygård, M. Hakala, S. Manninen, K. Hämäläinen, M. Itou, A. Andrejczuk, and Y. Sakurai, *Ion hydration studied by x-ray Compton scattering*, Physical Review B **73**, 024208 (2006).

[120] I. Juurinen, K. Nakahara, N. Ando, T. Nishiumi, H. Seta, N. Yoshida, T. Morinaga, M. Itou, T. Ninomiya, Y. Sakurai, *et al.*, *Measurement of two solvation regimes in Water-Ethanol mixtures using X-Ray compton scattering*, Physical review letters **107**, 197401 (2011).

[121] X. Yuan, Y. Zhang, T. A. Abtew, P. Zhang, and W. Zhang, *VO_2: Orbital competition, magnetism, and phase stability*, Phys. Rev. B **86**, 235103 (2012).

[122] T. T. Fister, D. D. Fong, J. A. Eastman, H. Iddir, P. Zapol, P. H. Fuoss, M. Balasubramanian, R. A. Gordon, K. R. Balasubramaniam, and P. A. Salvador, *Total-Reflection Inelastic X-Ray Scattering from a 10-nm Thick* $La_{0.6}Sr_{0.4}CoO_3$ *Thin Film*, Phys. Rev. Lett. **106**, 037401 (2011).

[123] N. Ogawa, K. Miyano, M. Hosoda, T. Higuchi, C. Bell, Y. Hikita, and H. Y. Hwang, *Enhanced lattice polarization in $SrTiO_3/LaAlO_3$ superlattices measured using optical second-harmonic generation*, Phys. Rev. B **80**, 081106 (2009).

[124] H. Hwang, Y. Iwasa, M. Kawasaki, B. Keimer, N. Nagaosa, and Y. Tokura, *Emergent phenomena at oxide interfaces*, Nature materials **11**, 103 (2012).

[125] T. Asmara, A. Annadi, I. Santoso, P. Gogoi, A. Kotlov, H. Omer, M. Motapothula, M. Breese, M. Rübhausen, T. Venkatesan, and A. Rusydi, *Mechanisms of charge transfer and redistribution in $LaAlO_3/SrTiO_3$ revealed by high-energy optical conductivity*, Nature communications **5**, (2014).

[126] A. Bosak and M. Krisch, *Phonon density of states probed by inelastic x-ray scattering*, Physical Review B **72**, 224305 (2005).